Finite Element Analysis of Voronoi Cellular Solids

by

Surekha Vajjhala

B.S. Materials Science and Engineering
Massachusetts Institute of Technology, 1996

Submitted to the Department of Materials Science and Engineering in Partial
Fulfillment of the Requirements for the Degree of

Master of Science
in
Materials Science and Engineering

June 1999

© 1999 Massachusetts Institute of Technology.
All rights reserved.

Signature of Author..
Department of Materials Science and Engineering
May 7, 1999

Certified by ....
Lorna J. Gibson
Matoula S. Salapatas Professor of Materials Science and Engineering
Thesis Supervisor

Accepted by ....
Linn W. Hobbs
John F. Elliott Professor of Materials
Chairman, Departmental Committee on Graduate Students

MASSACHUSETTS INSTITUTE
OF TECHNOLOGY
JUL 30 1999
LIBRARIES

Science

Finite Element Analysis of Voronoi Cellular Solids

by

Surekha Vajjhala

Submitted to the Department of Materials Science on May 7, 1999 in Partial
Fulfillment of the Requirements for the Degree of Master of Science in Materials
Science and Engineering

ABSTRACT

Finite element analysis (FEA) was used to study the mechanical behavior of three idealized cellular solids: a regular hexagon, a two-dimensional non-periodic honeycomb, and a three-dimensional random network of struts. FEA results for uniaxial deformation of the hexagon with elastic-plastic cell walls were compared to analytical solutions for stiffness and strength. A plastic failure envelope was calculated for the two-dimensional non-periodic honeycomb under biaxial loading. Results were compared to the failure envelope for a regular hexagonal honeycomb. Finally, FEA results for a three-dimensional random structure under cyclic compression were compared to experimental results for fatigue of trabecular bone. The studies demonstrated the usefulness of the unit cell approach and the strengths of different finite element models for understanding mechanical response to uniaxial, biaxial, and cyclic loading.

Thesis Supervisor: Lorna J. Gibson
Title: Matoula S. Salapatas Professor of Materials Science and Engineering

Acknowledgements

I once heard that graduate school is like being handed a small piece of the universe with the directive: "Solve this." Certainly, the thesis advisor's part in whether or not the student gets a solution is significant. But after sharing my own experiences with fellow students, I also recognize the critical role that an advisor plays in the overall quality of graduate school life. I was fortunate. I am very grateful to Professor Lorna Gibson for her guidance and enthusiastic support during my two years in the Department. A great big thanks to Ann Jacoby for suggesting her as an advisor.

I am indebted to a number of people for assistance with the software programs used in chapters 3 and 4, specifically Dr. Matt Silva and Grant Schaffner for the mesh generation code for the two-dimensional Voronoi honeycomb; Drs. John Sullivan and Ken Brakke for help installing their programs; and most of all, Dr. Andy Kraynik and his colleagues at Sandia National Laboratories for the software to build the three-dimensional Voronoi meshes. Andy, thank you for your patient instruction and attention to detail.

This research was supported by the Beinecke Brothers Memorial Scholarship, the Sperry Fund, and NIH grant #AR41894-0182. Special thanks to Dr. Tom Parkinson and Diego Gonzales for their assistance in administering these funds.

I am grateful to everyone at the Beth Israel Deaconess Medical Center Orthopedic Biomechanics Laboratory—especially Jon Conta and Dave Rosler for listening to all my stories. A special thanks to Manan Trivedi, who always reminded me of the bigger picture, and to my brother Raghav, who warned me on the first day that FEM is a bad idea for a thesis topic.

Finally, a note to my parents who always encouraged me to pursue my studies with passion and discipline: Your unconditional support of my personal and professional decisions has given me self-confidence and courage to embrace uncertainty. Thank you for the exciting opportunities that lie ahead.

Table of Contents

List of Figures and Illustrations

Chapter 2: Uniaxial mechanical properties of a regular hexagonal honeycomb

Chapter 3: A failure envelope for two-dimensional Voronoi honeycombs

Chapter 4: Fatigue of trabecular bone

List of Tables

Chapter 3: A failure envelope for two-dimensional Voronoi honeycombs

Chapter 4: Fatigue of Trabecular bone

List of Symbols

a	crack length
a_0	initial crack length
da/dN	crack growth rate
A_s, n_s	material creep constants
$\Delta A/A$	change in area divided by initial area
b	depth of hexagonal honeycomb members
d	diameter of trabecular strut cross section
DOF	degrees of freedom
δ_a	axial deflection of horizontal members of hexagon
E_s	Young's modulus of the solid
E_x^*	Young's modulus in the x-direction
E_y^*	Young's modulus in the y-direction
ε_x	strain in x-direction
ε_y	strain in y-direction
F_x	reaction force in x-direction
F_y	reaction force in y-direction
G	strain energy release rate
h	strain-hardening coefficient
I	moment of inertia
K	bulk modulus
K_{com} (K_{ten})	bulk moduli for compression (tension)
K_{hex} (K_{Vor})	bulk moduli for hexagonal (Voronoi) honeycombs
K_I, K_{II}, K_{III}	stress intensity factors in opening, sliding, and tearing modes
l	length of cell wall
L_x	length of cellular solid in x-direction
L_y	length of cellular solid in y-direction
M	external bending moment
$\langle M \rangle_c$ ($\langle M \rangle_t$)	average bending moment in compression (tension)
M_i	bending moment for ith element
μ	shear modulus
NE	total number of cell edges
N_f	number of cycles to failure
ν_s	Posson's ratio for the solid
r	radius of trabecular strut cross section
RF	reaction force
R_{fcc}	radius of fcc cyrstal lattice
ρ^*/ρ_s	relative density
$\langle S \rangle_c$ ($\langle S \rangle_t$)	average axial force in compression (tension)
SF1	axial reaction forces
S_i	axial force for ith element

SM1, SM2	section bending moments
SM3	section twisting moment
$\Delta\sigma/E_0$	normalized stress range
σ_b	bending moment
σ_t	axial stress
σ_x^*, $\sigma_{x,failure}$	yield strength in the x-direction
σ_x, σ_1	stress in x-direction
σ_y^*, $\sigma_{y,failure}$	yield strength in the y-direction
σ_y, σ_2	stress in y-direction
σ_{ys}	yield strength of the solid
t	thickness of cell wall
θ	angle at vertex of hexagon
τ_m	twisting moment
U_x	displacement in x-direction
U_y	displacement in y-direction

1 Introduction

1.1 Background

A cellular solid is "made up of an interconnected network of solid struts or plates which form the edges and faces of cells (Gibson and Ashby, 1997)." Examples from nature include bees' honeycombs, cork, coral, and wood. In the last decade, there has been a remarkable increase in applications and manufacturing techniques for cellular solids. Man-made examples range from prismatic honeycombs in catalytic converters to Triscuit wafers. Cellular solids have a variety of applications such as sandwich panels in airframe structures and foamed polymers for insulation. Understanding the mechanical properties of cellular solids can lead to improved materials design and performance.

Analytical and numerical solutions for the behavior of cellular solids have been developed using two- and three-dimensional geometric models for open and closed cells (Gibson and Ashby, 1997). Some models have been extended to understand the properties of specific cellular solids like foams and trabecular bone (Beaupre and Hayes, 1985; Guo et al, 1994; Kraynik et al, 1997; Silva and Gibson, 1997). Numerical solutions allow parametric studies than cannot be easily obtained from experimental data. Finite element models are useful for predicting and interpreting the micromechanical consequences of various external loading configurations.

In this study we develop computational models to explore the mechanical behavior for three idealized cellular solids: a unit cell of a regular two-dimensional hexagonal honeycomb, a random two dimensional non-periodic honeycomb, and a random three dimensional non-periodic open cellular solid. We extend the results of the final model and apply them to a physically meaningful problem, namely fatigue of trabecular bone.

1.2 Objectives

There were three principal aims for this study:

1. to demonstrate the usefulness of finite element analysis (FEA) and the unit cell approach,
2. to understand the biaxial loading behavior of a random cellular solid, and
3. to compare the fatigue behavior of a random three-dimensional cellular solid model to the behavior of trabecular bone under cyclic compression.

1.3 Overview

Chapter 2 demonstrates the use of the unit cell approach and finite element analysis (FEA) to compute the uniaxial properties of a regular hexagonal honeycomb. A comparison to the closed-form solutions for elastic modulus and plastic yield strength enables us to evaluate the effectiveness of the finite element approach.

In chapter 3, we perform FEA to obtain a plastic failure envelope or yield surface for a non-periodic, two-dimensional random honeycomb. We study bending and stretching in the cell walls to understand the differences between the periodic and non-periodic biaxial loading behavior.

Chapter 4 extends the idealized non-periodic model to three dimensions. We apply the model to represent a specific cellular solid, trabecular bone. By selecting physically meaningful input parameters, we study micro-mechanisms for osteoporotic fracture in trabecular bone, in particular the micro-mechanical response to fatigue.

1.4 References

Beaupre GS and Hayes WC. Finite element analysis of a three-dimensional open-celled model for trabecular bone. *J. Biomech. Eng.* 1985; **107**: 249-256.
Gibson LJ and Ashby MF. Cellular Solids Structure and Properties. Cambridge University Press, 1997.
Guo XE, McMahon TA, Keaveny TM, Hayes WC and Gibson LJ. Finite element modeling of damage accumulation in trabecular bone under cyclic loading. *J. Biomech.* 1994; **27**: 145-155.
Kraynik AM, Neilsen MK, Reinelt DA, and Warren WE. Foam Micromechanics: Structure and Rheology of Foams, Emulsions, and Cellular Solids. Proceedings of the NATO Advanced Study Institute on "Foams, Emulsions, and Cellular Materials." Kluwer, 1997.
Silva MJ and Gibson LJ. Modeling the mechanical behavior of vertebral trabecular bone: effects of age-related changes in microstructure. *Bone* 1997; **21**: 191-9.

2 Uniaxial mechanical properties of a regular hexagonal honeycomb

2.1 Background

Man-made honeycombs are commercially available for an assortment of applications: polymer and metal honeycombs for structural applications, metal ones for energy-absorbing applications, and ceramic ones for high-temperature processing. Understanding the properties of honeycombs allows us to define new applications and improve design parameters for existing applications. Characterizing the mechanical behavior of two-dimensional honeycombs is also important because the results shed light on the mechanics of complex three-dimensional foams.

Analytical model

Gibson et al (1982) derived an analytical expression for Young's modulus for a unit hexagonal cell by calculating the moment required to bend a cell wall and the resulting deflection. For a regular hexagonal honeycomb (figure 1) with linear elastic walls of uniform thickness, t, side length, l, and Young's modulus, E_s, the expressions for in-plane Young's moduli reduce to

$$\frac{E_x^*}{E_s} = \frac{E_y^*}{E_s} = \frac{4}{\sqrt{3}}\left(\frac{t}{l}\right)^3, \qquad (1)$$

where E_x^* and E_y^* are Young's moduli in the x- and y-directions, respectively. The thickness to length ratio, t/l is given as a function of the relative density ρ^*/ρ_s by

$$\left(\frac{t}{l}\right) = \frac{\sqrt{3}}{2}\left(\frac{\rho^*}{\rho_s}\right). \tag{2}$$

If one includes axial and shear deflections, which become especially significant when (t/l) > 0.2, the expression for Young's moduli of a regular hexagonal honeycomb becomes

$$E^*_x = E^*_y = \frac{4}{\sqrt{3}} E_s \left(\frac{t}{l}\right)^3 \frac{1}{1+(5.4+1.5\nu_s)\left(\frac{t}{l}\right)^2}. \tag{3}$$

Note that this expression reduces to equation 1 for small t/l.

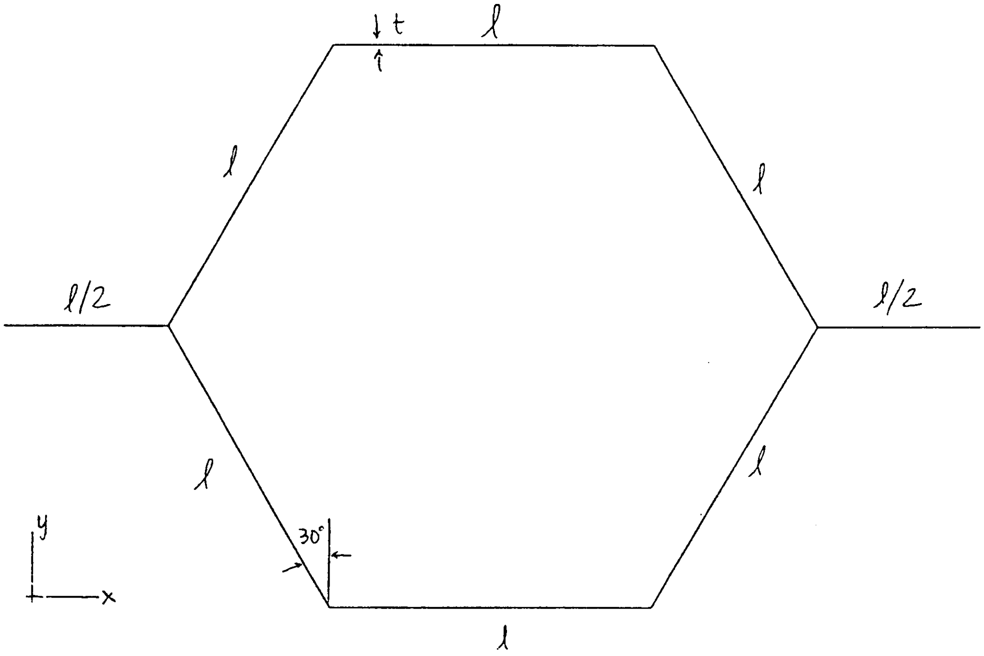

Figure 1: A regular hexagonal unit cell with cell walls of length, l and thickness, t.

Gibson et al (1982) also gave an analytical expression for the yield strength of a hexagonal unit cell with elastic-perfectly plastic cell walls. Elastic buckling precedes plastic collapse so long as

$$\left(\frac{t}{l}\right) < 3\frac{\sigma_{ys}}{E_s}.$$

Otherwise, plastic collapse occurs when the bending moment in the cell walls reaches the fully plastic moment. When the two moments are equated, the plastic yield stress of the regular hexagon reduces to

$$\frac{\sigma_x^*}{\sigma_{ys}} = \frac{\sigma_y^*}{\sigma_{ys}} = \frac{2}{3}\left(\frac{t}{l}\right)^2. \tag{4}$$

Our research aim in this study was to show that finite element analysis (FEA) can be used to compute mechanical properties for a regular hexagonal honeycomb. After demonstrating that the computational results are consistent with analytical solutions, we can extend the study to understand mechanical behavior of non-periodic honeycombs, which are less well understood.

2.2 Methods

Analytical evaluation of mechanical properties

Young's modulus and uniaxial yield strength were determined for a regular hexagonal honeycomb of relative density, ρ^*/ρ_s=0.15. The elastic-perfectly plastic cell wall properties were Young's modulus, E_s=1.0, Poisson's ratio, ν_s=0.3, yield strength, σ_{ys}=0.01, and thickness to length ratio, t/l=0.13. Using the equations 3 and 4 discussed above, we obtained the following results:

$$E_x^*/E_s=E_y^*/E_s=E^*/E_s=4.61 \times 10^{-3}$$

$$\sigma_x^*/\sigma_{ys}=\sigma_y^*/\sigma_{ys}=\sigma_{pl}^*/\sigma_{ys} = 1.13 \times 10^{-2}.$$

Finite Element Analysis

Unit cell mesh generation

To compute the mechanical properties of a regular hexagonal honeycomb, FEA input files were created for a regular hexagonal honeycomb unit cell. Four to eight three-noded elements (ABAQUS beam type B22) comprised each cell wall of length, l, uniform thickness, t, and width, b (ABAQUS, Hibbitt, Karlsson, & Sorensen, Inc., Pawtucket, RI). The cell wall properties and value of t/l were identical to those given above. The selected mesh consisted of 32 elements and 64 nodes. The results of a convergence study (figure 2) showed that the reaction force in the displacement direction came within 3.7% and 1.6% of the exact solution in the x and y directions, respectively.

Computing uniaxial mechanical properties using FEA

Young's modulus and uniaxial compressive yield strength were computed for both x and y directions. To determine the Young's modulus and yield strength in the x direction (figure 3), a displacement in the x-direction was imposed on node C in one step. Node F was constrained from translating in the x direction. Rotation in the x-y plane was prevented at nodes A, B, D, E, G, and H to reproduce the behavior of a unit cell in a hexagonal honeycomb (figure 3b). A node on wall CD was constrained from translating in the x-direction to ensure uniform deformation of the unit cell. Reaction forces and displacements were reported for the displaced node at each increment.

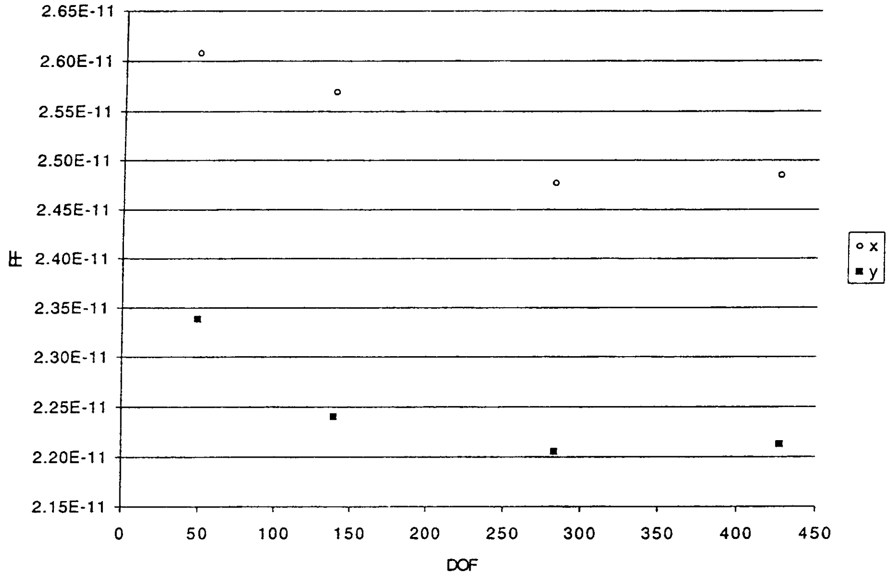

Figure 2: Convergence study results. Reaction forces were plotted against the number of degrees of freedom to determine how many degrees of freedom were required to achieve convergence for testing in both x- and y-directions Each point on a series corresponds to a different mesh.

The Young's modulus and yield strength in the y-direction were determined by imposing a vertical displacement on nodes A and B, while nodes G and H were prevented from translating in the y-direction. To represent behavior in a hexagonal honeycomb, nodes A, B, D, E, G, and H in the unit cell were prevented from rotating in the x-y plane (figure 3c). One node on wall AB was constrained from translating in the x-direction to ensure uniform deformation of the unit cell. Reaction forces and displacements were reported for the displaced nodes at each increment.

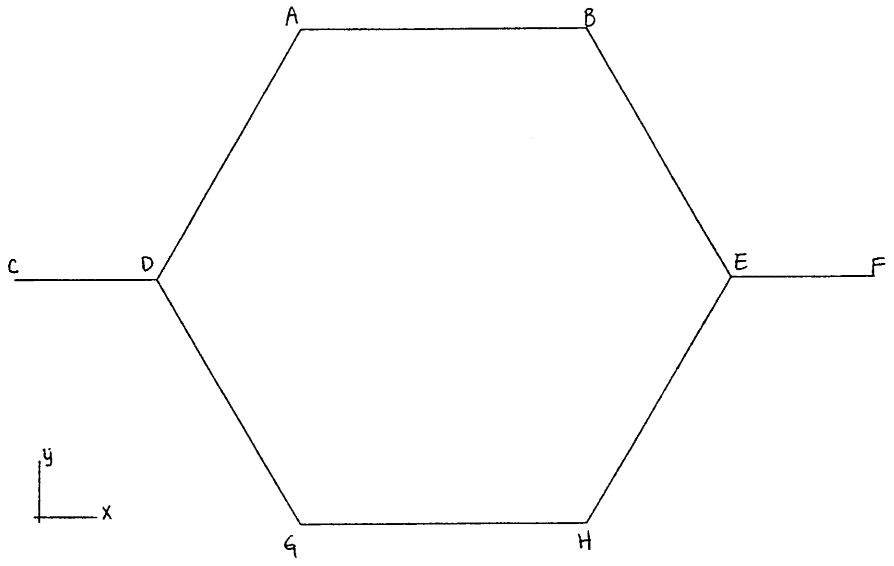

Figure 3: (a) The initial finite element mesh for the unit cell of a hexagonal honeycomb

Stress, σ and strain, ε were calculated from the reported reaction forces, F and displacements, U at each increment using the following expressions (figure 4):

$$\sigma_x = \frac{F_x}{2bl\cos\theta} \tag{5a}$$

$$\varepsilon_x = \frac{U_x}{2(l + l\sin\theta)} \tag{5b}$$

$$\sigma_y = \frac{F_y}{2b(l + l\sin\theta)} \tag{6a}$$

$$\varepsilon_y = \frac{U_y}{2l\cos\theta} \tag{6b}$$

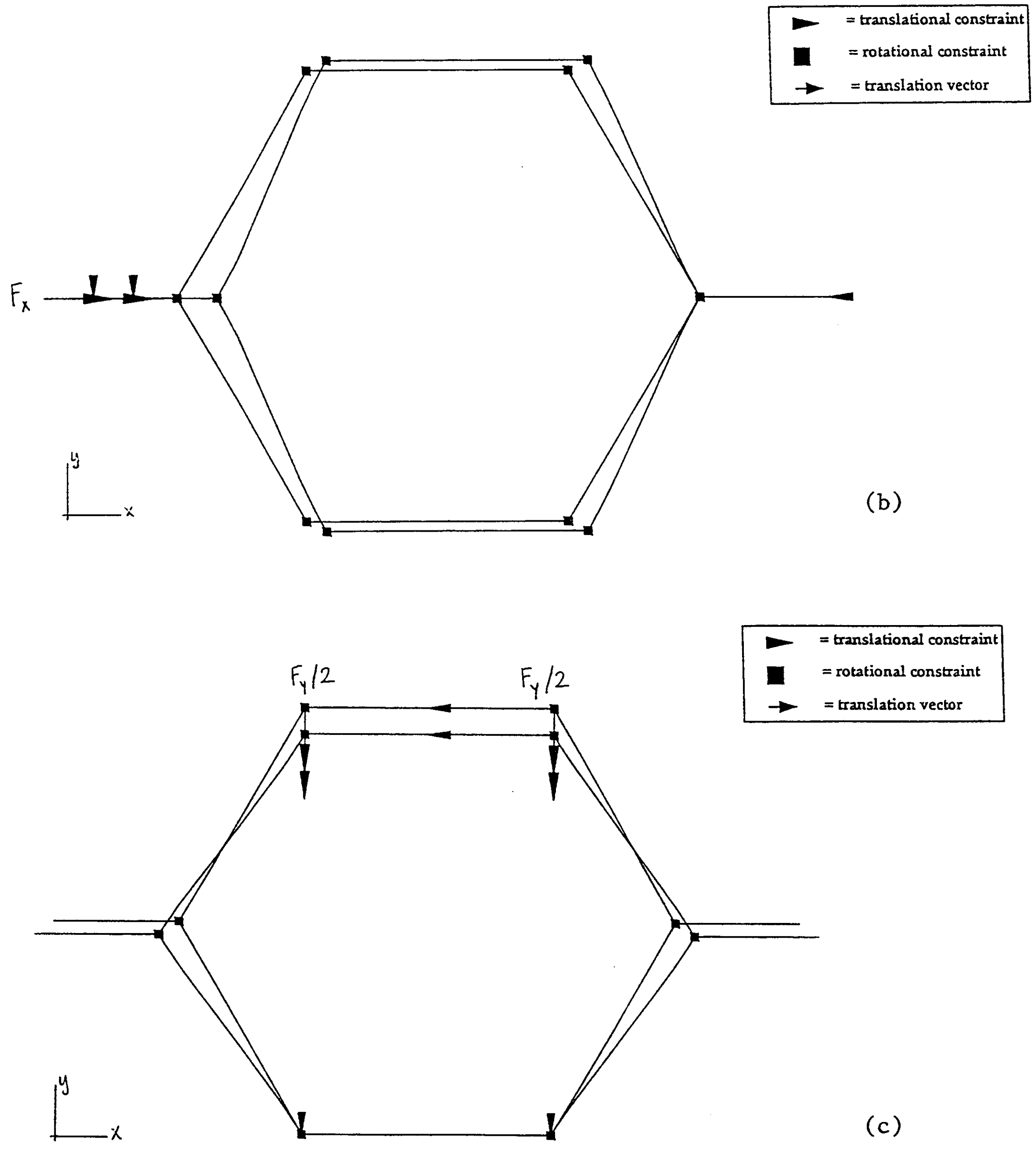

Figure 3: Boundary conditions used to determine E* and σ_{ys} in the (b) x- and (c) y-directions. The arrowheads represent translational constraints, and the squares represent rotational constraints. Displacement boundary conditions are denoted by arrows with tails.

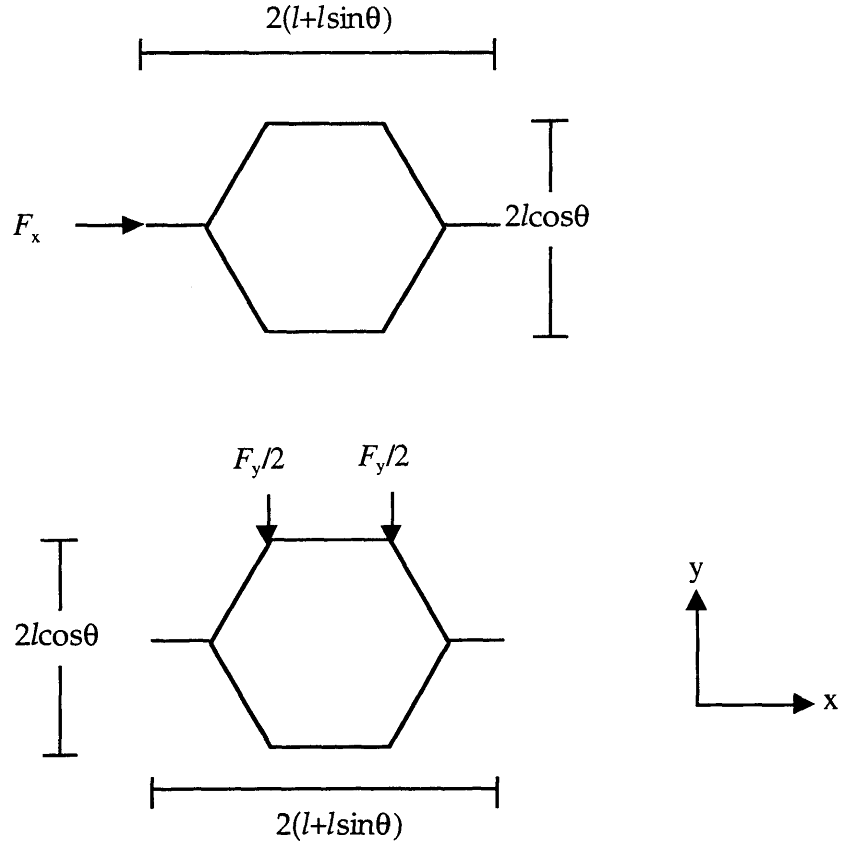

Figure 4: Calculation of stress and strain in the x- and y-directions.

Young's Modulus, E^* was calculated for both x- and y-directions by computing the tangent to the stress-strain curve at the second increment of load so that

$$E_x = \frac{\sigma_{x,1}}{\varepsilon_{x,1}} \tag{7a}$$

$$E_y = \frac{\sigma_{y,1}}{\varepsilon_{y,1}} \tag{7b}$$

Uniaxial yield strength was taken as the peak value of stress on a stress-strain curve.

2.3 Results

Analytical values for uniaxial mechanical properties

Evaluation of analytical expressions for mechanical properties of an isotropic hexagonal honeycomb with linear elastic-perfectly plastic cell wall material (E_s=1.0, ν_s=0.3, σ_{ys}=0.01, t/l=0.13) gave the following results:

$$E_x^*/E_s=E_y^*/E_s=E^*/E_s=4.61 \times 10^{-3}$$

$$\sigma_x^*/\sigma_{ys}=\sigma_y^*/\sigma_{ys}=\sigma_{pl}^*/\sigma_{ys} = 1.13 \times 10^{-2}.$$

Uniaxial mechanical properties by FEA

Uniaxial properties were also computed based on a finite element analysis of a unit hexagonal cell with linear elastic-perfectly plastic cell wall material. Stress-strain curves for the x- and y-directions are shown below (figure 5). Young's modulus and yield stress were calculated for both directions giving the following results:

$$E_x^*/E_s=4.64 \times 10^{-3}$$

$$E_y^*/E_s=4.59 \times 10^{-3}$$

$$\sigma_x^*/\sigma_{ys}=1.21 \times 10^{-2}$$

$$\sigma_y^*/\sigma_{ys}=1.10 \times 10^{-2}.$$

2.4 Discussion

We developed a finite element model for a unit cell of a hexagonal honeycomb to compare the computational predictions of Young's modulus and failure strength to

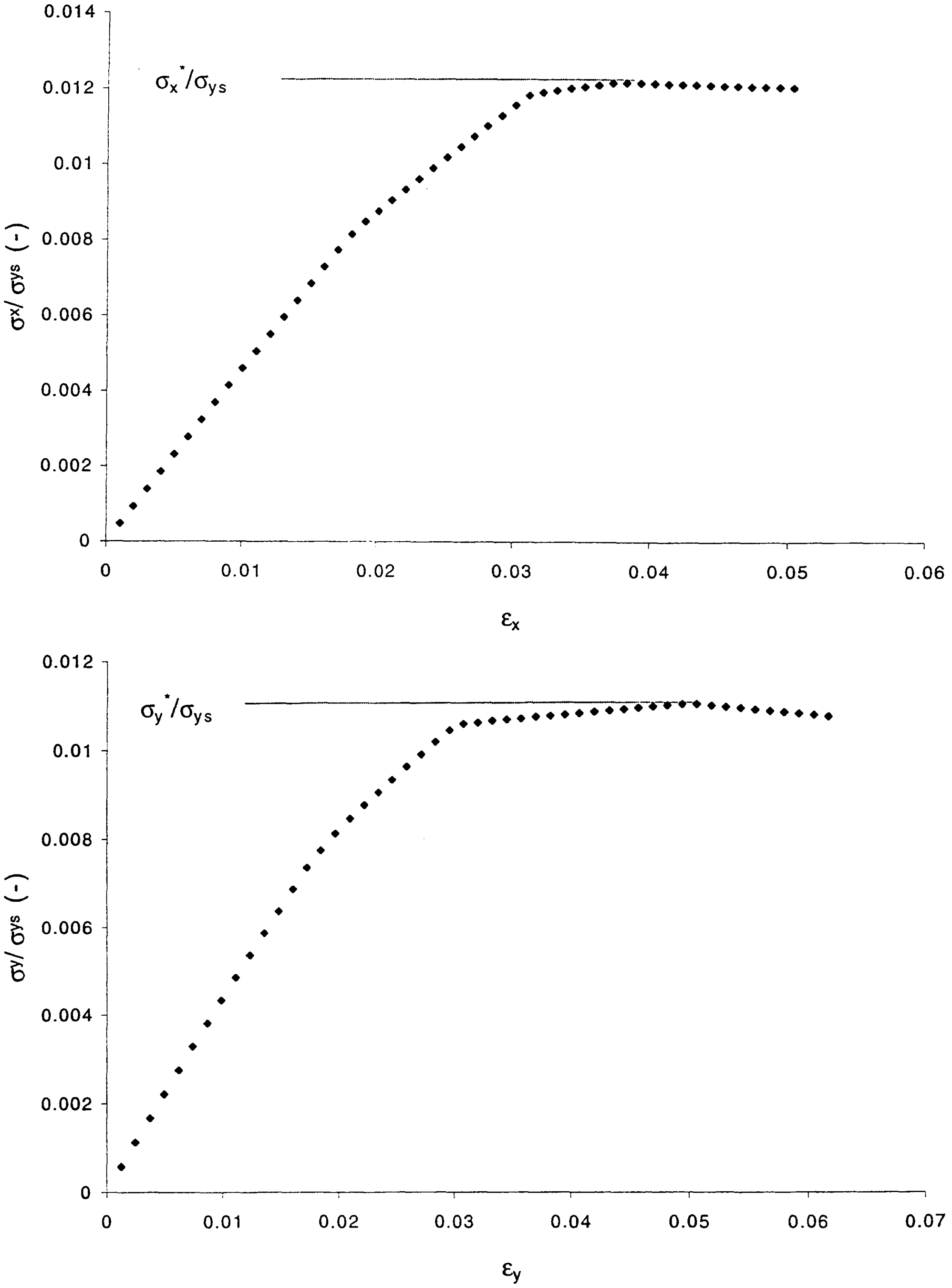

Figure 5: Young's modulus and yield stress were determined from stress-strain curves for the (a) x- and (b) y-directions of the hexagonal unit cell.

the values obtained using analytical expressions. The computational findings are largely in agreement with analytical results.

Finite element analysis results for Young's modulus in the two directions differed from the analytical values by 0.6% and -0.4% in the x- and y-directions, respectively. We expect $E_x = E_y$ for regular hexagonal structures, and the FEA results give Young's Moduli which differ by only 1%. An explanation for the difference between Young's moduli in the x- and y-directions for the model and the analytical solution is that the analytical solution (equation 3) assumes that the walls AB, CD, EF, and GH have thickness t/2 as they would in a proper unit cell. We assigned identical thickness, t to the walls in our "unit" cell. For loading in the y-direction, walls AB, CD, EF, and GH are unloaded so E_y should be nearly equal to the analytical results. However, for deformation in the x-direction, axial loading in walls AB and GH is included in the finite element calculations. Then the axial deflection δ_a for these members in our model is:

$$\delta_a = \frac{Fl}{btE_s} \tag{8}$$

Gibson and Ashby (1997) give small strain calculations of the moduli, including axial and shear deformations. Accounting for the thicker walls, the analytical solution for Young's modulus in the x-direction becomes

$$E_x^* = E_s\left(\frac{t}{l}\right)^3 \frac{\left(\frac{h}{l}+\sin\theta\right)}{\cos^3\theta}\,\frac{1}{\left[1+\left(2.4+1.5\nu_s+\tan^2\theta+\frac{(h/l)}{\cos^2\theta}\right)\left(\frac{t}{l}\right)^2\right]} \tag{9}$$

Evaluating this expression for our model gives Young's modulus in the x-direction $E_x^*/E_s= 4.71\times10^{-3}$. The FEA result for stiffness differs from this value by –1.49%.

We also expect strength to be equal in both x- and y-directions for the regular hexagonal unit cell. When comparing the computational and analytical results for plastic yield strength, one should consider boundary conditions, mesh design, and element types. To mimic behavior of a unit cell in a periodic lattice, rotational boundary constraints were imposed at the hexagon nodes for loading in the two directions as shown in figure 3. In addition, each cell wall of length l was modeled with the same number of elements. A finer mesh or a mesh with varying numbers of elements per cell wall might have improved the accuracy of our solution. Selection of the element types could also improve the results. A continuum model would approach the analytical solution more exactly. These factors may explain the 7.1% and 2.7% differences between the x- and y-direction yield strengths, respectively, and the yield strength as determined by the analytical expressions.

2.5 Conclusions

This study demonstrated that a finite element model can be effectively used to evaluate Young's modulus and plastic yield strength for a hexagonal honeycomb unit cell. Improvements to this study should focus on a better evaluation of yield strength by FEM.

2.6 Reference

Gibson LJ, Ashby MF, Schajer GS, and Robertson CI. *Proc. R. Soc. Lond.* 1982; **A382**: 25.

3 A failure envelope for two-dimensional Voronoi honeycombs

3.1 Background

Behavior of cellular solids in uniaxial loading is relatively well understood. However, loads in real engineering structures are often multiaxial. For these cases, the designer is concerned less with the uniaxial stress than with the combination of stresses causing failure. In this chapter we consider failure i.e the onset of plasticity of a two-dimensional non-periodic cellular solid subject to biaxial loads.

Biaxial properties can be studied by considering the plastic moments and axial forces in cell walls of a cellular solid. The biaxial properties of periodic structures like the regular hexagonal honeycomb have been analyzed (Gibson et al, 1989). In the case of equibiaxial stress states, the plastic moments cancel so that the cell walls stretch. In this extreme, the axial stresses in the cell wall define the criteria for plastic failure. To obtain the complete failure surface for a hexagonal honeycomb, Gibson et al (1989) considered both stretching and bending of cell walls. Their analytical solution for the plastic yield surface of a hexagonal honeycomb gives two intersecting ellipses following the equations:

$$\pm\left[\frac{\sigma_1\left(\frac{h}{l}+\sin\theta\right)\sin\theta-\sigma_2\cos^2\theta}{\left(t/l\right)^2}\right]=\frac{\sigma_{ys}}{2}\left\{1-\left[\frac{\sigma_1\left(\frac{h}{l}+\sin\theta\right)\cos\theta+\sigma_2\cos\theta\sin\theta}{\sigma_{ys}\left(t/l\right)}\right]^2\right\}. \qquad (1)$$

For regular hexagonal cells, the failure envelope delineating plastic collapse is the intersection of two symmetric elongated ellipses (figure 1).

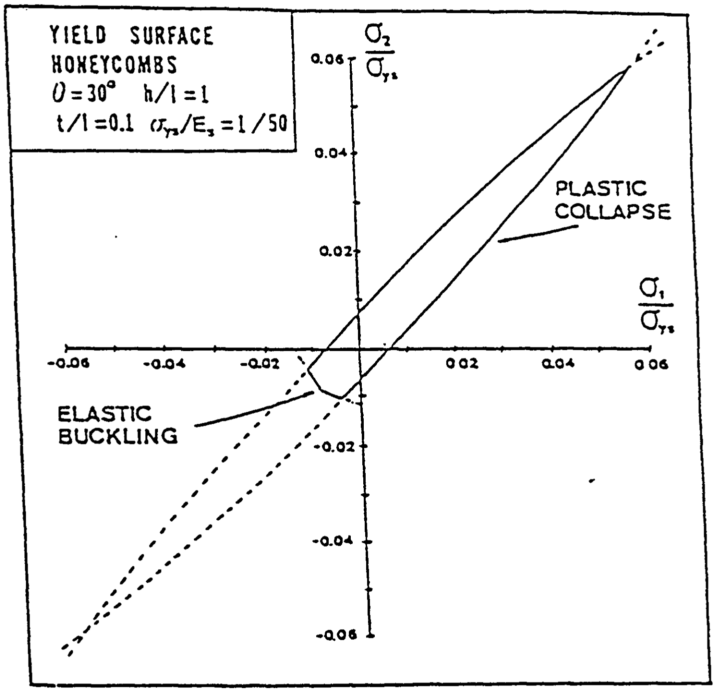

Figure 1: The plastic yield surface for an idealized, two-dimensional cellular solid made up of regular hexagonal cells. The surface is truncated by the elastic buckling failure surface in biaxial compression. (from Gibson et al, 1989)

While the biaxial failure envelope for regular hexagonal honeycombs has been determined analytically, the multiaxial loading behavior of random honeycombs and foams is less well understood. An exact analytical solution for the random non-periodic structure of foams cannot be obtained. A finite element model for a Voronoi cellular solid would enable one to study bending and stretching in the cell walls of a random, non-periodic structure.

The Voronoi honeycomb is constructed as follows. Consider points distributed randomly in a plane. If at each point a gas bubble were to nucleate simultaneously and grow radially at the same rate, then the initial structure would be a Voronoi honeycomb. Alternatively, the structure can be thought of as a network composed of the perpendicular bisectors of line segments connecting each point to its nearest neighbors (figure 2). By excluding points within a specified distance, or "exclusion distance," one can create a relaxed Voronoi honeycomb, a more regular structure.

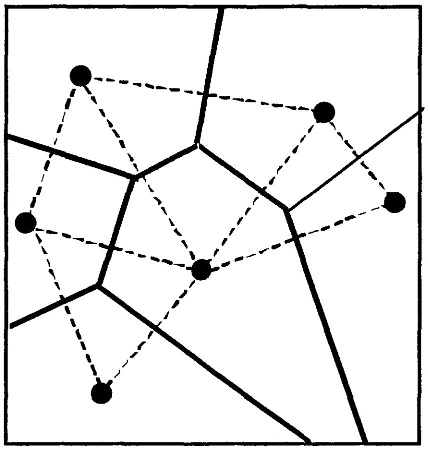

Figure 2: Cell centers are randomly distributed in a plane. Dotted lines connect each cell center to its nearest neighbors. The perpendicular bisectors, shown in solid lines, connect to give the resulting Voronoi honeycomb.

Depending on the relative density, the honeycombs can represent cellular solids, e.g. the result of spherulitic growth in some polymers. According to Gibson and Ashby (1997), the nearest thing to Voronoi honeycombs in nature include coral, some sponges, and the nests of wasps and ants.

Silva performed finite element analysis (FEA) to study the uniaxial properties of non-periodic cellular solids (Silva et al, 1995/Silva and Gibson, 1997). He determined that elastic properties could be well represented by combining estimates of relative density and microstructural anisotropy with simple relations developed for periodic honeycombs. For twenty isotropic Voronoi honeycombs with a relative density of 15%, the mean relative Young's modulus, $E^*/E_s=0.488 \times 10^{-2}$, was within a few percent of the analytical solution. Young's modulus varied as a power law of relative density with an exponent of approximately 2.5. This relationship nearly identically matched the results of a closed-form solution for the elastic modulus of a hexagonal honeycomb as described in the previous chapter (eqn 3). The uniaxial compressive strength of Voronoi honeycombs with a relative density of 15% was 30% lower than that of the corresponding regular hexagonal honeycomb. This finding contrasts sharply with the strongly correlated results for Young's modulus of the periodic and non-periodic structures.

Our goal in this study was to compute a failure envelope for an elastic-perfectly plastic 2D Voronoi cellular solid using FEA. By comparing our results to the failure behavior of a regular hexagonal honeycomb, we hoped to gain insight on the effect of non-periodic structure on the biaxial failure envelope.

3.2 Methods

Mesh generation

FEA input files for two-dimensional Voronoi honeycombs were produced using software originally written by Matt Silva (Silva, 1996). Each Voronoi mesh was constructed by connecting the perpendicular bisectors of line segments between adjacent "nucleation" points in two-space to form a network of cell walls.
To obtain a more even distribution of cell size, points within a specified exclusion distance were not considered nearest neighbors. For our 17x17 mesh, the exclusion distance was set at 2 units of length.

The original programs were modified to allow control over the number of finite elements in a cell wall. This feature was used to perform a convergence study (see Results) to identify the required number of degrees of freedom.

The final mesh had 309 cells (figure 3). Because the cells had no preferred orientation, the model was considered to be isotropic. Each cell wall had uniform thickness and was modeled as a series of four 3-noded beam elements (ABAQUS element type B22) with Young's Modulus, $E_S=1$, Poisson's ratio, $\nu_S=0.3$, and yield strength, $\sigma_{ys}=0.01$. The mesh tested in this study achieved a relative density ρ^*/ρ_S of 0.15 by specifying a uniform cell wall thickness which was computed using the expression:

$$\frac{\rho^*}{\rho_s} = \frac{\text{Area of Solid}}{\text{Total Area}} = \sum_{i=1}^{NE} \frac{l_i t}{L_x L_y}, \qquad (2)$$

where NE is the total number of cell edges, t is the uniform cell wall thickness, l_i is the length of the ith cell wall, and L_X and L_y are the dimensions of the cellular solid.

The mesh used for uniaxial and biaxial compression loading had elastic-perfectly plastic cell walls, while for uniaxial tension, biaxial tension, and combined tension-compression stress states, cell walls were modeled using strain-hardened material with a strain hardening coefficient, h=0.01 (figure 4). Though the elastic-perfectly plastic walls were sufficient to achieve failure in compression, slight strain-hardening was required to induce a discernible failure point in tension loading. A convergence study indicated that four elements per cell wall or 11,288 degrees of freedom were adequate to obtain a solution within 6% of the exact solution in both x and y directions (figure 5). The final mesh had 3836 nodes and 1988 elements.

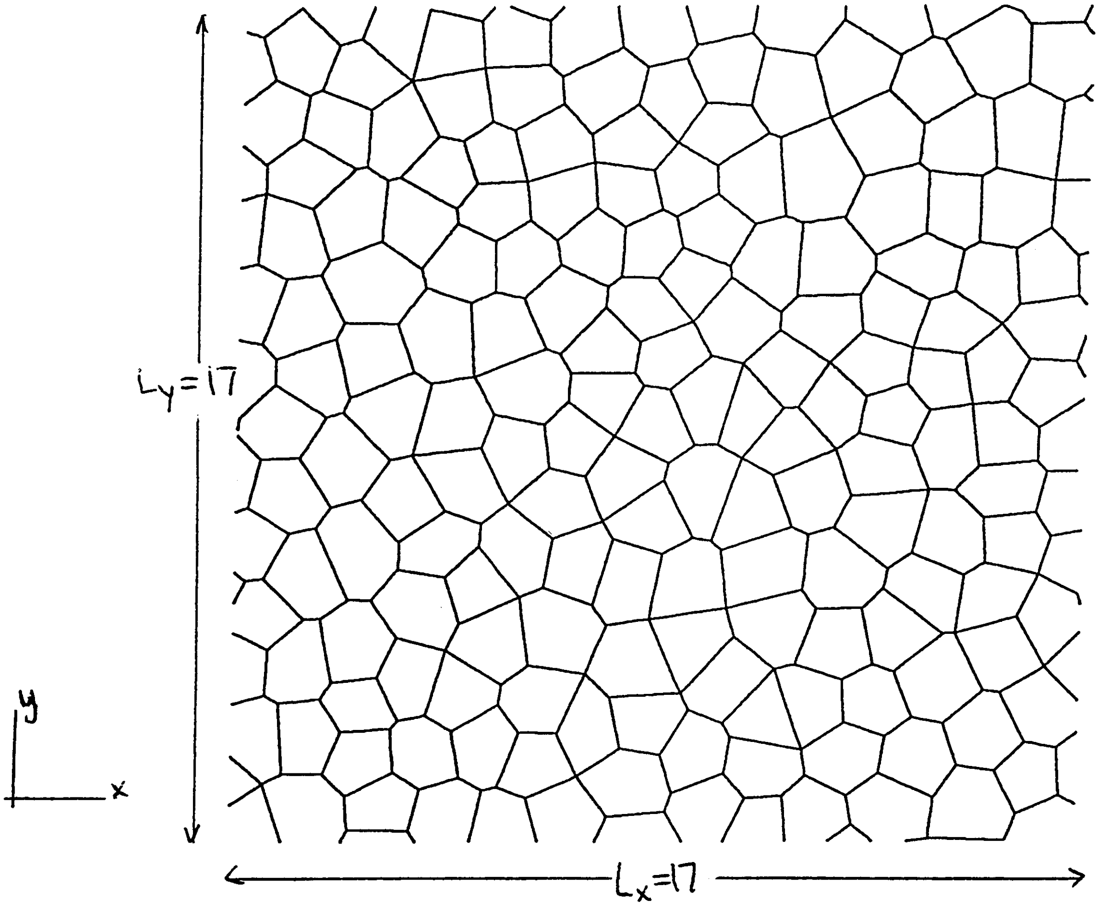

Figure 3: The Voronoi honeycomb finite element mesh had 309 cells.

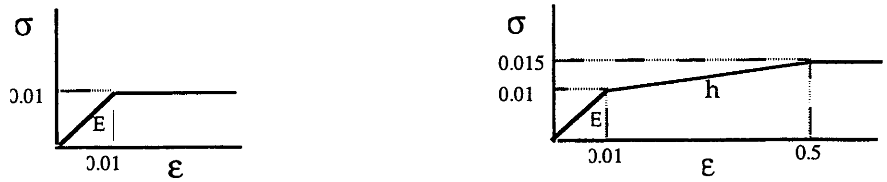

Figure 4: The cell wall material was modeled as elastic-perfectly plastic (a) for compression tests and as elastic-perfectly plastic with slight strain-hardening (b) for tension tests. Note that the schematics are not drawn to scale.

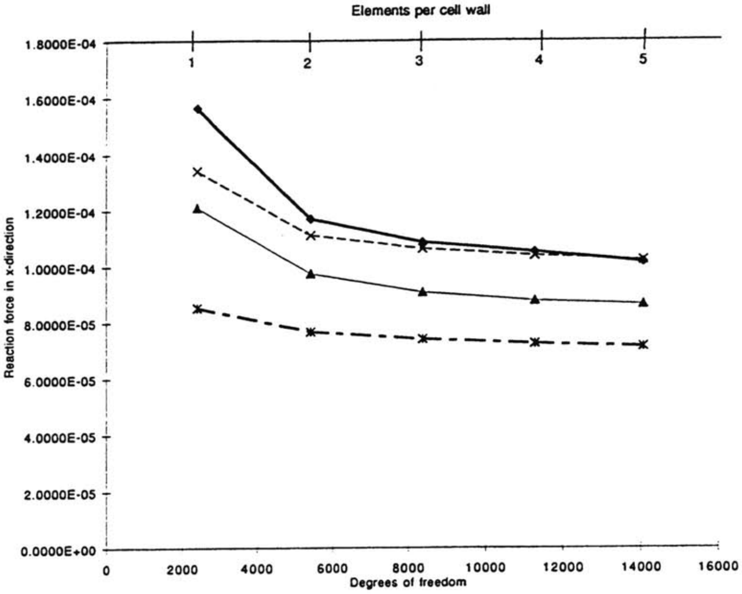

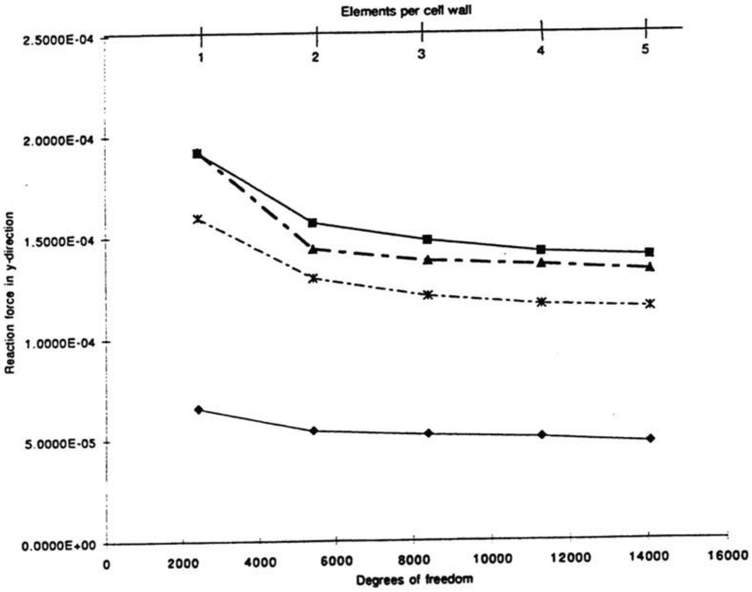

Figure 5: Convergence studies were conducted in both the x and y directions of the mesh. Each series of points corresponds to one node on the mesh. Each point of a series denotes the reaction force resulting from a prescribed displacement of the node for a model with a specified number of degrees of freedom in the mesh. The degrees of freedom were adjusted by controlling the number of elements per cell wall. Results indicated that four elements per cell wall were adequate.

Uniaxial properties

Elastic properties and the uniaxial yield strength of the Voronoi honeycomb were determined using a displacement boundary condition. The nodes forming an edge were displaced by a specified amount while the nodes of the opposite edge were prevented from translating in the direction of displacement. Additional boundary conditions were imposed to apply biaxial stresses. Since biaxial testing specified displacements at two edges, boundary conditions were ultimately imposed at all four edges for the biaxial tests. To design a uniaxial testing methodology that would be consistent with the anticipated biaxial testing, the nodes of one of the two edges in the direction normal to the displacement direction were prevented from translating in the direction normal to the displacement direction (figure 6). Edge nodes were prevented from rotating in the x-y plane to reduce local crushing effects. A mesh with edges free from rotation constraints was also tested for comparison.

Uniaxial deformation occurred in one step. Each step was automatically divided into increments. Uniaxial compression testing required approximately twenty increments to achieve a specified displacement while tension required about sixty increments. Stress and strain, or average displacement per length, were computed at each increment using the following expressions:

$$\sigma_{x_i} = \frac{\sum_{n=1}^{EN_x} RF_{x_n}}{L_y} \tag{3a}$$

$$\sigma_{y_i} = \frac{\sum_{n=1}^{EN_y} RF_{y_n}}{L_x} \tag{3b}$$

$$\varepsilon_{x_i} = \frac{\sum_{n=1}^{EN_x} U_{x_n}}{EN_x \cdot L_x} \tag{4a}$$

$$\varepsilon_{y_i} = \frac{\sum_{n=1}^{EN_y} U_{y_n}}{EN_y \cdot L_y} \tag{4b}$$

where i refers to the increment, n specifies a node, EN is the number of nodes in a displaced edge, RF is the reaction force at a node in a displaced edge, L_x and L_y are the edge lengths, and U is the specified displacement of each node on the edge. Strain is calculated by taking the average nodal displacement. Young's modulus was calculated using the stress and strain from the first increment of the uniaxial compression test:

$$E_x = \frac{\sigma_{x_1}}{\varepsilon_{x_1}} \tag{5a}$$

$$E_y = \frac{\sigma_{y_1}}{\varepsilon_{y_1}}. \tag{5b}$$

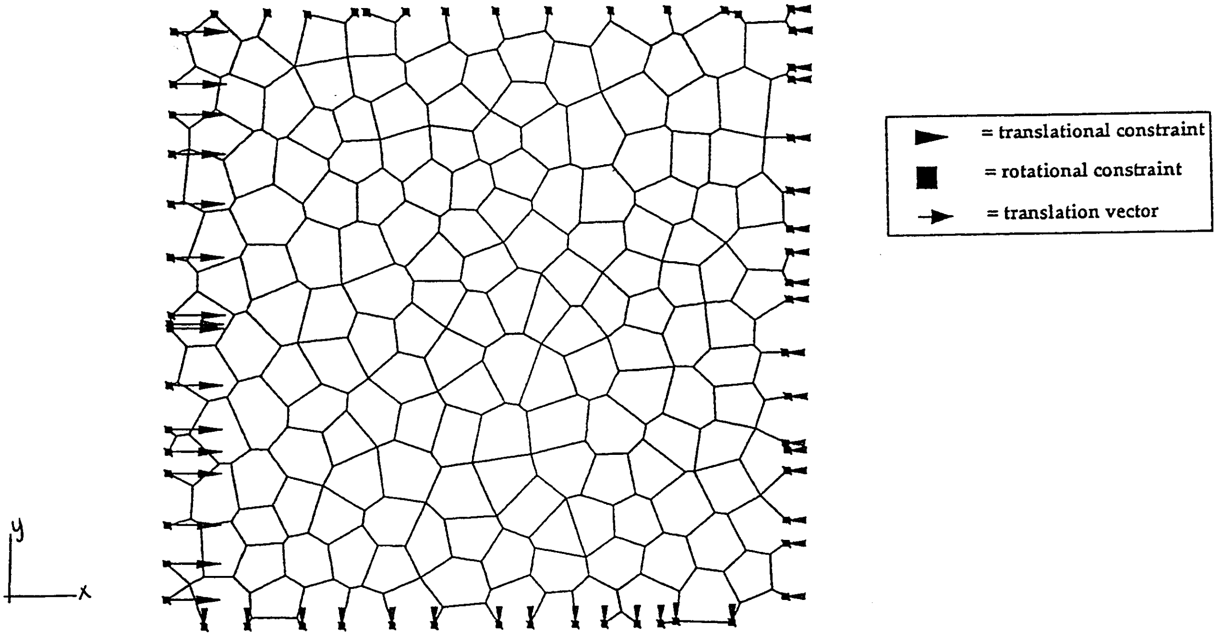

Figure 6: This figure depicts boundary conditions used to determine E^* and σ^* in the x-direction for the Voronoi honeycomb. The squares and arrowheads represent rotational constraints at edge nodes and translational constraints, respectively. Arrows with tails indicate displacements.

For compression, yield strength was taken as the peak value of stress on the stress-strain curve (figure 7a). For tensile testing, yield strength was taken as the intercept of the linear elastic and plastic portions of the stress-strain curve (figure 7b).

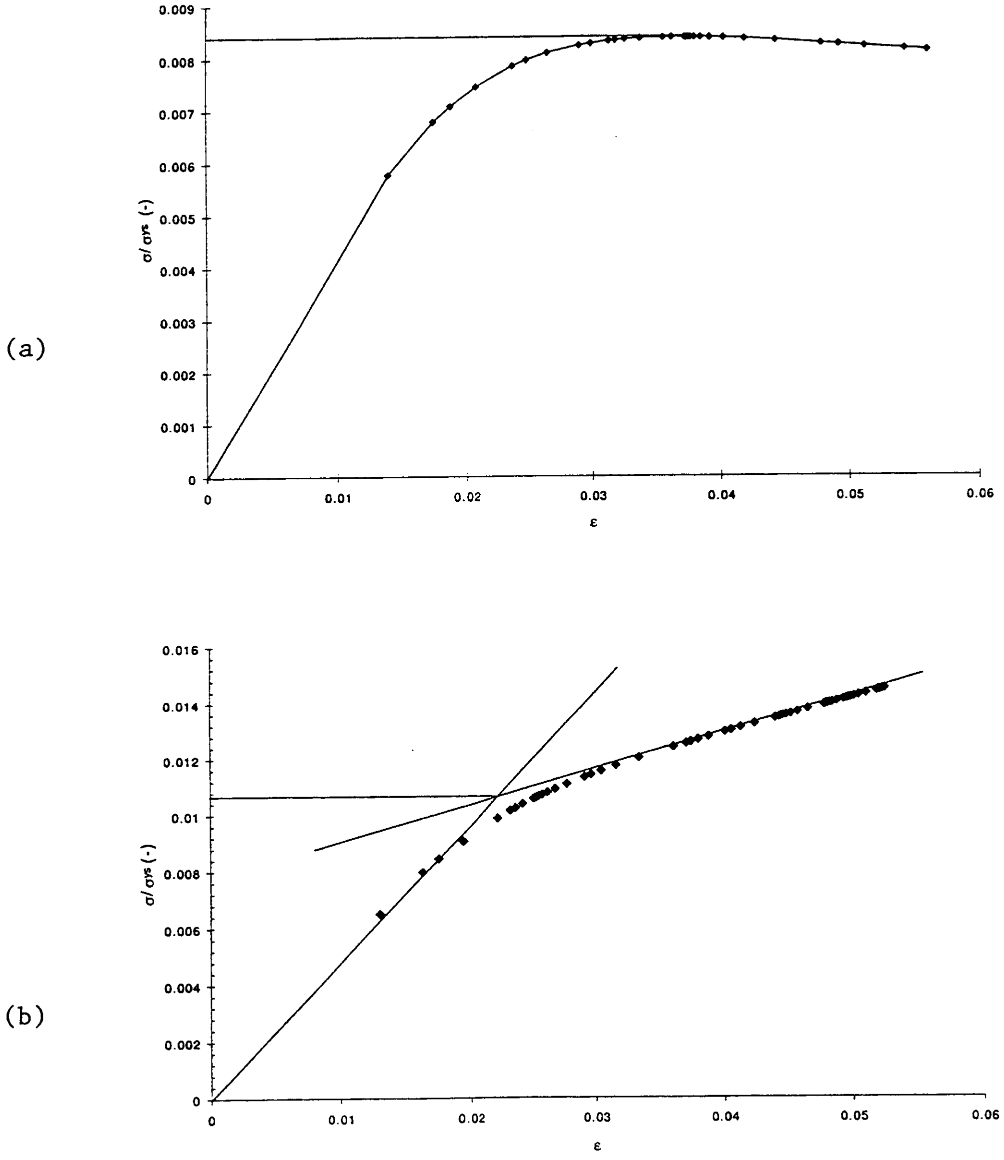

Figure 7: Uniaxial yield strength was taken as the peak of a stress-strain curve for compression (a) and as the intercept of the linear elastic and plastic portions for tension (b).

Biaxial properties

Biaxial deformation required two steps. The first step occurred as in uniaxial deformation except that the displacement magnitude was limited to strains in the linear-elastic portion of the stress-strain curve. In the second step, the edge displaced in the first step was prevented from translating further in its original displacement direction while a displacement boundary condition was applied in the second direction to the fourth edge (which had no prior translational constraints). Stress was computed at both of the displaced edges in their respective displacement directions at each increment and plotted against the strain associated with the edge displaced in the second step (figures 8 and 9). Failure corresponded to a peak or the intercept of the linear elastic and plastic portions on one of the stress-strain curves. The combination of stresses served as coordinates for a point on the failure envelope. The magnitudes of displacements in the first and second steps were varied to obtain twenty points on the two-dimensional failure envelope.

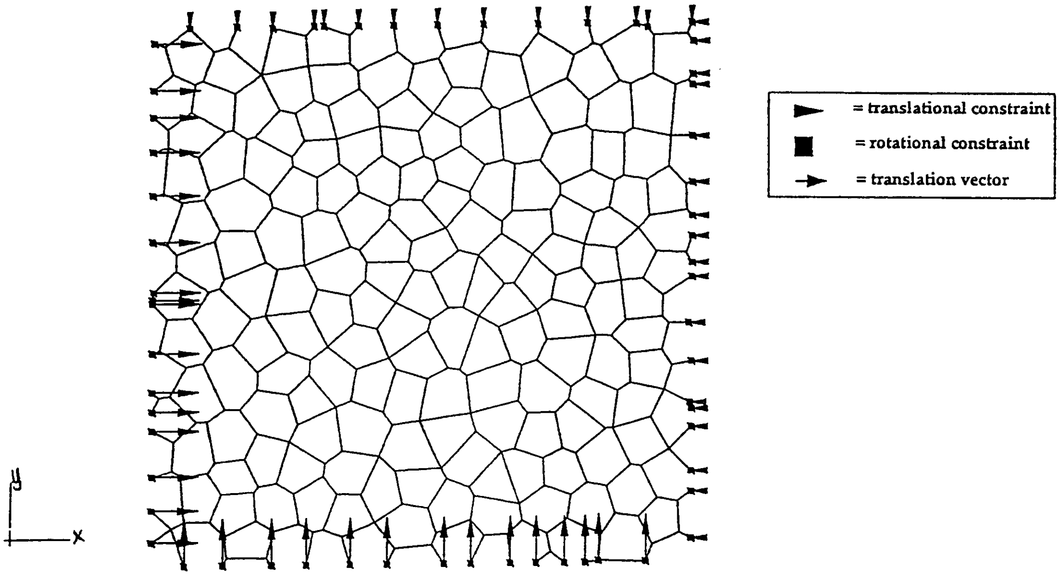

Figure 8: Squares indicate that rotation was prevented in the x-y plane at a node. Arrowheads denote a restriction in translation in one direction at a node. Arrows indicate direction and magnitude of displacement.

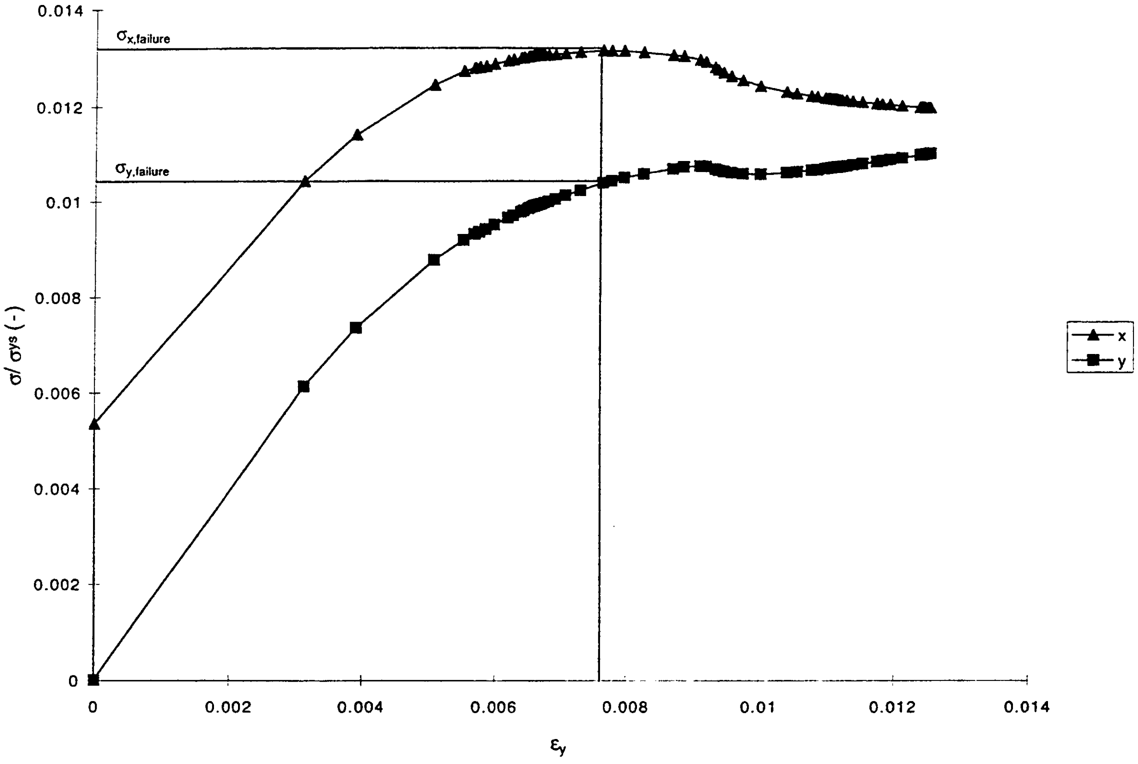

Figure 9: Stress was plotted for both directions against the strain at increments in the second step. The first peak in the stress-strain curves indicated the yield strength in one direction, shown here as $\sigma_{x,failure}$. The corresponding stress, shown here as $\sigma_{y,failure}$, was taken as the yield strength in the second direction.

Element moment and stress characterization

Section forces and geometry were used to calculate internal moments and stresses for each element. Bending moments, M_i and axial forces, S_i, were obtained for each element in equibiaxial tension and compression to characterize bending and stretching contributions to failure in each mode.

Bulk modulus

The bulk modulus, K, was computed using results from equibiaxial compression and tension of a mesh with the same geometry but with linear elastic cell walls. The following expression was used:

$$K = \frac{\Delta\sigma}{\Delta A/A}, \tag{6}$$

where $\Delta\sigma$ is the equibiaxial compressive stress, ΔA is the change in area, and A is the initial area. The mesh was also deformed beyond failure to depict visually the elastic cell walls in equibiaxial tension and compression.

For comparison, the bulk modulus was calculated for a regular hexagonal honeycomb using the following expressions:

$$\begin{aligned} &A_0 = l^2 \\ &A = (l-\delta)^2 = l^2 - 2\delta l + \delta^2 \approx l^2 - 2\delta l \\ &\frac{\Delta A}{A_0} = \frac{A - A_0}{A_0} = \frac{-2\delta}{l} \approx 2\varepsilon \\ &K = \frac{\Delta\sigma}{\Delta A/A} = \frac{\Delta\sigma}{2\Delta\varepsilon} = \frac{E_s\left(t/l\right)}{2\sqrt{3}} \end{aligned} \tag{7}$$

3.3 Results

Uniaxial Stiffness and Strength

Young's Modulus was computed for both x- and y-directions in compression giving the following results:

$$E_x^*/E_s = 4.42 \times 10^{-3}$$

$$E_y^*/E_s = 4.13 \times 10^{-3},$$

where E_i^* is Young's Modulus in the i-direction and E_s is Young's Modulus for the cell wall material.

Yield strength was computed for both x- and y-directions in uniaxial compression and tension with the following results:

$$\sigma_{xc}^* / \sigma_{ys} = 8.89 \times 10^{-3}$$

$$\sigma_{yc}^* / \sigma_{ys} = 8.39 \times 10^{-3}$$

$$\sigma_{xt}^* / \sigma_{ys} = 11.0 \times 10^{-3}$$

$$\sigma_{yt}^* / \sigma_{ys} = 9.90 \times 10^{-3},$$

where σ_{ic}^* is the compressive yield strength in the i-direction, σ_{it}^* is the tensile yield strength in the i-direction, and σ_{ys} is the yield strength of the cell wall material. FEM and analytical solutions for Young's modulus and uniaxial strength are shown for the regular hexagonal honeycomb and for the Voronoi honeycomb in Table 1.

Table 1: Mechanical properties of periodic and non-periodic honeycombs

	Regular hex, analytical solution	Regular hex, FEM solution	Voronoi, FEM solution
E_x	4.61×10^{-3}	4.64×10^{-3}	4.42×10^{-3}
E_y	4.61×10^{-3}	4.59×10^{-3}	4.13×10^{-3}
K	0.037	*	0.020
$\sigma_{x,c}$	1.13×10^{-2}	1.21×10^{-2}	0.889×10^{-2}
$\sigma_{y,c}$	1.13×10^{-2}	1.10×10^{-2}	0.839×10^{-2}
$\sigma_{x,t}$	1.13×10^{-2}	*	1.10×10^{-2}
$\sigma_{y,t}$	1.13×10^{-2}	*	0.990×10^{-2}

*not determined

Failure Envelope Results

The locus of points defining yield strength for twenty combinations of biaxial strain was plotted to create the failure envelope (figure 10). Three sets of points were plotted. The first set was derived for a Voronoi mesh with an elastic-perfectly plastic cell wall material. The second set of points corresponds to a Voronoi mesh with strain hardened cell wall material. Whereas the first two sets were derived for a mesh with restricted x-y rotation at the edge nodes, the third set was derived for a Voronoi mesh with perfectly plastic cell wall material but with edge nodes free from x-y rotation constraints. For each point (σ_x,σ_y), σ_x was normalized by the uniaxial compressive yield strength in the x-direction and σ_y was normalized by the uniaxial compressive yield strength in the y-direction. Each set of points was normalized by the uniaxial compressive yield strengths obtained for that set to allow comparison between sets. Values of the coordinates are given in Table 2.

Table 2a: Failure stress values for biaxial compression of Voronoi honeycomb with elastic-perfectly plastic cell walls and edge nodes with rotational constraints.

σ_x	σ_y
0	$-8.39\text{x}10^{-5}$
$-8.87\text{x}10^{-5}$	0
$-9.92\text{x}10^{-5}$	$-12.1\text{x}10^{-5}$
$-10.6\text{x}10^{-5}$	$-12.2\text{x}10^{-5}$
$-11.6\text{x}10^{-5}$	$-12.2\text{x}10^{-5}$
$-11.6\text{x}10^{-5}$	$-12.2\text{x}10^{-5}$
$-12.7\text{x}10^{-5}$ *	$-12.2\text{x}10^{-5}$*
$-12.7\text{x}10^{-5}$	$-7.81\text{x}10^{-5}$
$-12.8\text{x}10^{-5}$	$-8.60\text{x}10^{-5}$

-13.0x10^{-5}	-12.1x10^{-5}
-13.1x10^{-5}	-11.5x10^{-5}
-13.1x10^{-5}	-11.3x10^{-5}
-13.2x10^{-5}	-10.4x10^{-5}

*equibiaxial strength in compression

Table 2b: Failure stress values for Voronoi honeycomb with strain-hardened cell walls and edge nodes with rotational constraints.

σ_x	σ_y
-13.1x10^{-5}	-12.5x10^{-5}
-5.34x10^{-5}	3.29x10^{-5}
2.30x10^{-5}	-5.80x10^{-5}
0	9.90x10^{-5}
10.6x10^{-5}	0
14.9x10^{-5}*	15.0x10^{-5}*
14.9x10^{-5}	16.7x10^{-5}
16.4x10^{-5}	14.0x10^{-5}
16.7x10^{-5}	18.3x10^{-5}
17.0x10^{-5}	15.6x10^{-5}
19.0x10^{-5}	14.5x10^{-5}

*equibiaxial strength in tension

Table 2c: Failure stress values for Voronoi honeycomb with unconstrained edge nodes. Compression loading was done using elastic-perfectly plastic cell walls; tension loading was done using strain-hardened cell walls.

σ_x	σ_y
0	-6.18x10^{-5}
-7.11x10^{-5}	0

-6.96×10^{-5}	-6.49×10^{-5}
14.4×10^{-5}	14.0×10^{-5}

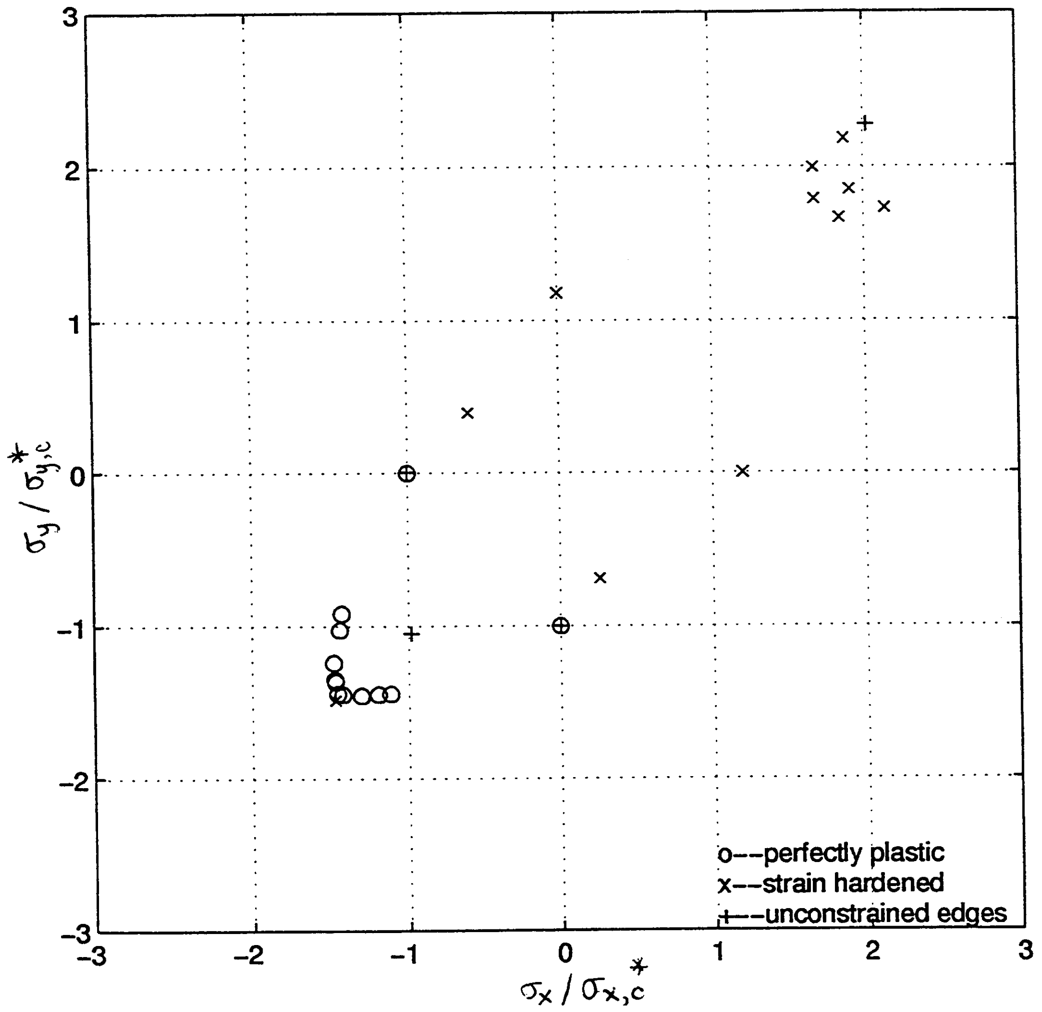

Figure 10a: Three sets of points were plotted to produce the plastic failure envelope for a Voronoi honeycomb. Points marked by "o" and "x" correspond to a Voronoi mesh with rotational constraints at edge nodes having elastic-perfectly plastic and elastic-strain hardened cell walls, respectively. Points marked by "+" represent results for a mesh with no edge constraints. Each set of points was normalized by the uniaxial compressive yield strength for the set. Deformation of the cell walls could not be seen at the stresses used for the analysis.

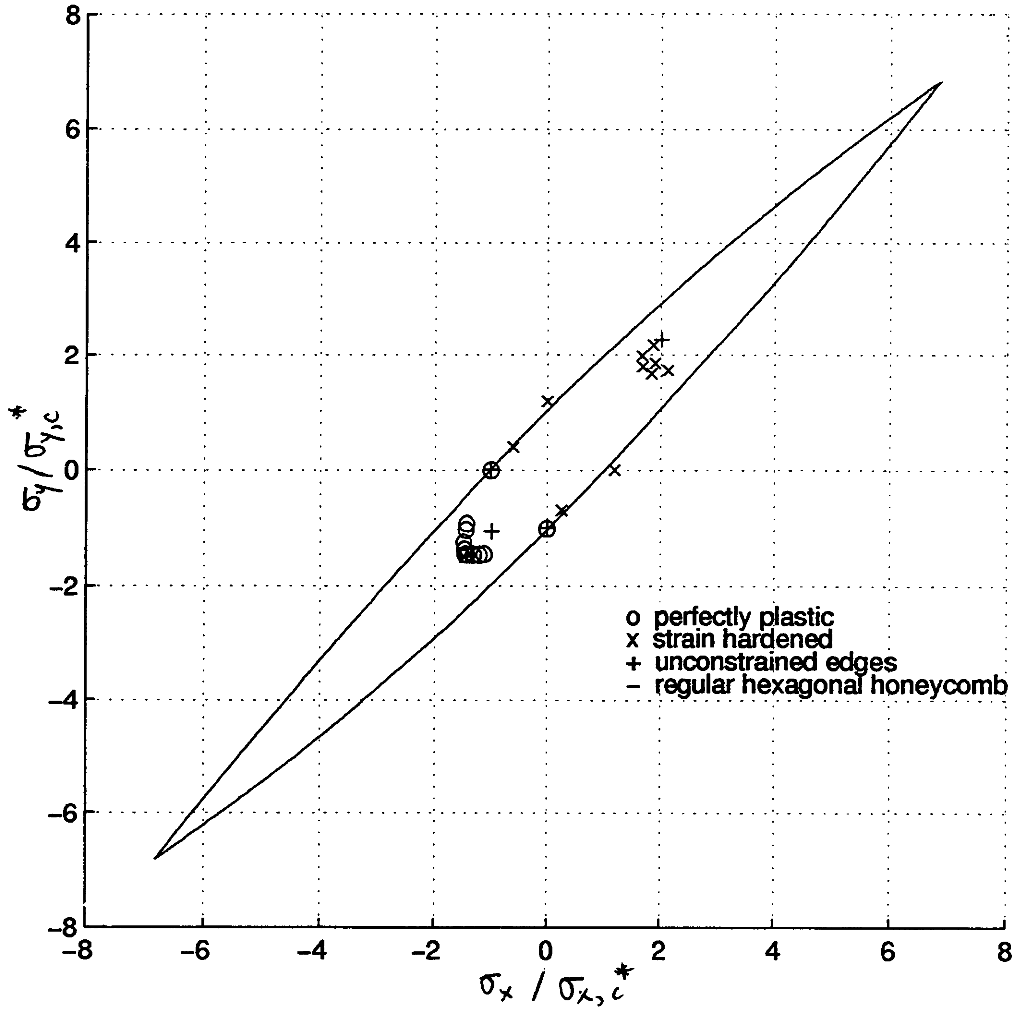

Figure 10b: The three sets of points are shown with the plastic failure envelope for a regular hexagonal honeycomb following equation (1) where $\theta=30°$, $h/l=1$, $t/l=0.13$, and $\sigma_{ys}/E_s=0.01$.

Axial Forces in Elements

Axial forces were computed for each element in the mesh for two stress states: equibiaxial compression and equibiaxial tension (see the * values in Tables 2a and 2b). These cases corresponded to the equibiaxial strengths on the plastic failure envelope. The average axial force in compression (1.131×10^{-6}) was very close to the value obtained in tension (1.135×10^{-6}), and the distribution of axial forces was also similar for the two stress states. To compare the distributions, data was plotted in the histogram shown below (figure 11).

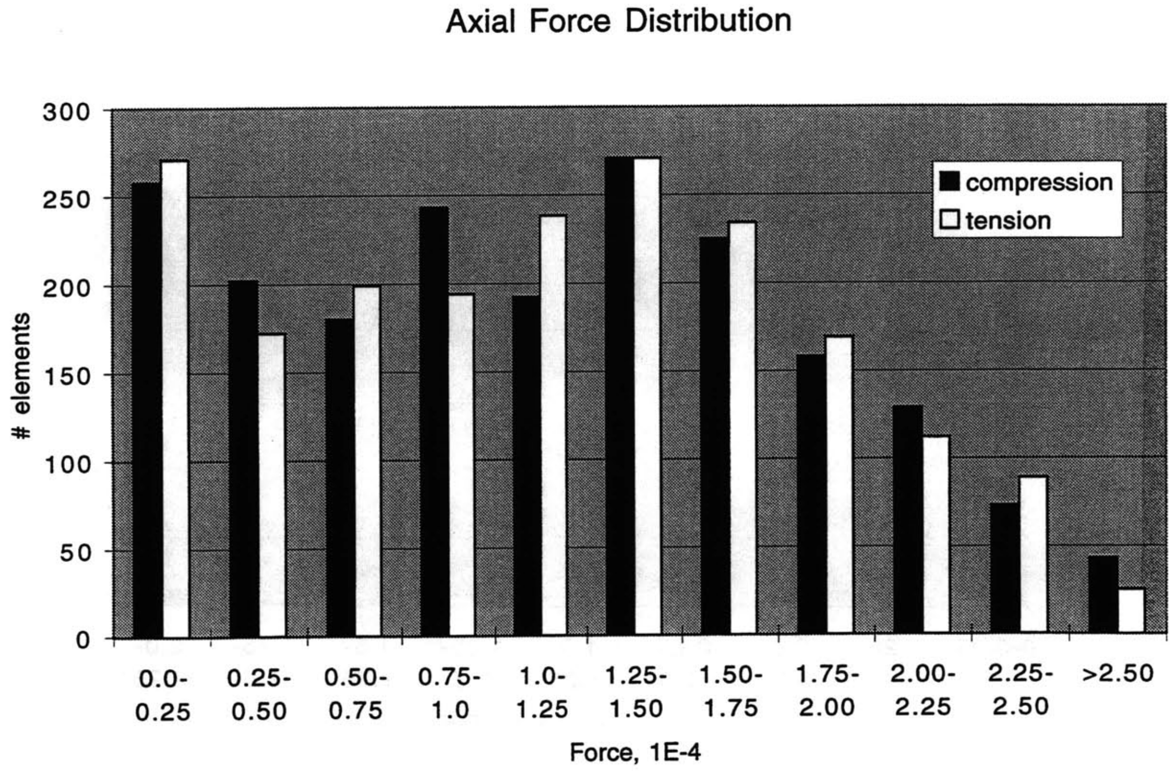

Figure 11: This histogram compares the distribution of axial forces in the cell walls of a Voronoi mesh in equibiaxial tension and in equibiaxial compression.

Element Section Moments

Section moments were also computed for each cell wall in equibiaxial compression and tension (see the * values in Tables 2a and 2b). The average element section moment for compression was 4.241×10^{-6} while the value for tension was 2.279×10^{-6}. The distribution results, depicted in the following histogram (figure 12), show that more elements have greater moments in compression than in tension.

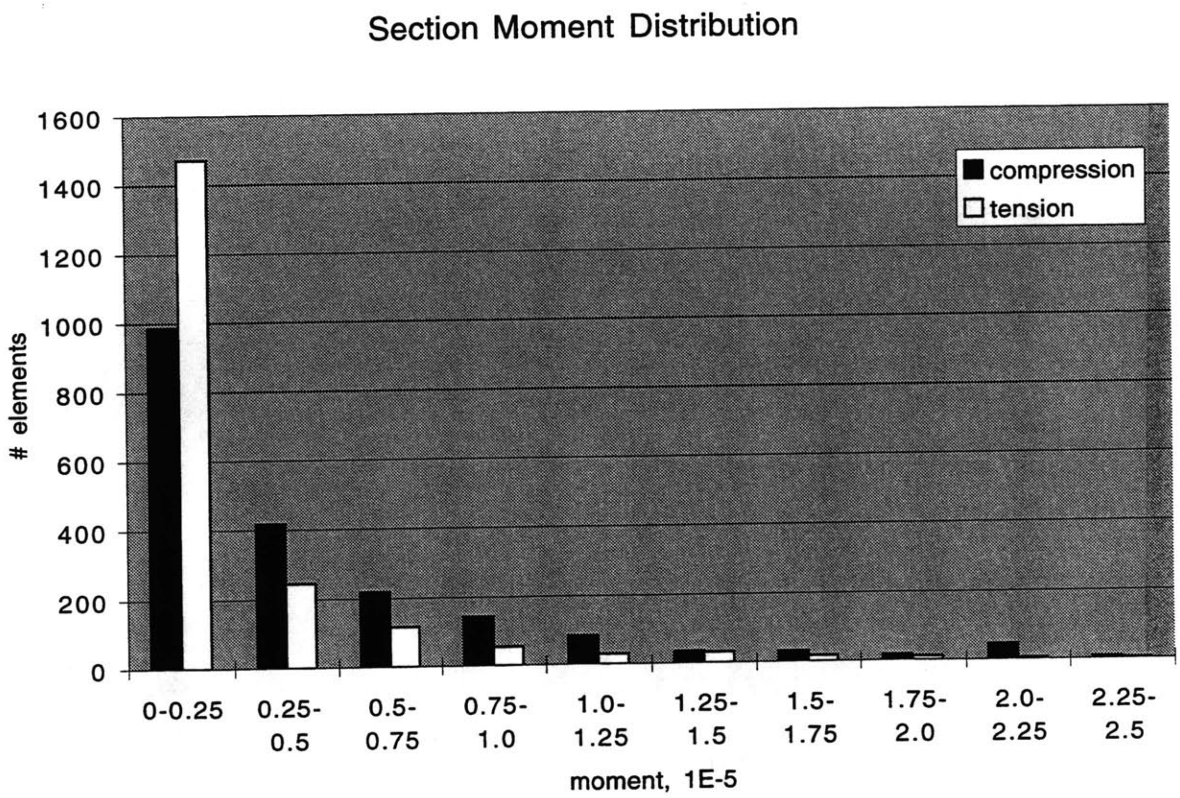

Figure 12: This histogram shows a comparison of the section moment distribution for elements of a Voronoi mesh in equibiaxial compression and in equibiaxial tension.

Bulk Modulus

Bulk modulus calculations were made using the same Voronoi mesh but with linear elastic cell wall material. Stresses in the x- and y-directions were plotted against the strain at each increment of the second step of biaxial compression. The stress value $\Delta\sigma$ used to calculate bulk modulus, K, was chosen at an increment for which the stress values in the x- and y-directions were equal (figure 13). This point corresponded to biaxial strain of approximately 0.02%. The Voronoi mesh used in this study had $K_{com}=1.98 \times 10^{-2}$ and $K_{ten}=2.01 \times 10^{-2}$.

Bending of the linear elastic cell walls was evident when the initially 17x17 model was compressed to dimensions of 16x16 (figure 14a). In contrast to the compression results, individual cell walls stretched to achieve equibiaxial tension (from 17x17 to 18x18—figure 14b).

Evaluation of the analytical expressions for bulk modulus of a hexagonal honeycomb gave a result of $K^*/E_s=0.037$.

3.4 Discussion

We conducted finite element analysis of a Voronoi honeycomb to compute a plastic failure envelope for an idealized cellular solid. We compared Young's modulus, uniaxial strength, and biaxial failure envelopes of Voronoi and regular hexagonal honeycombs to identify and understand differences attributed to the non-periodic structure of foams.

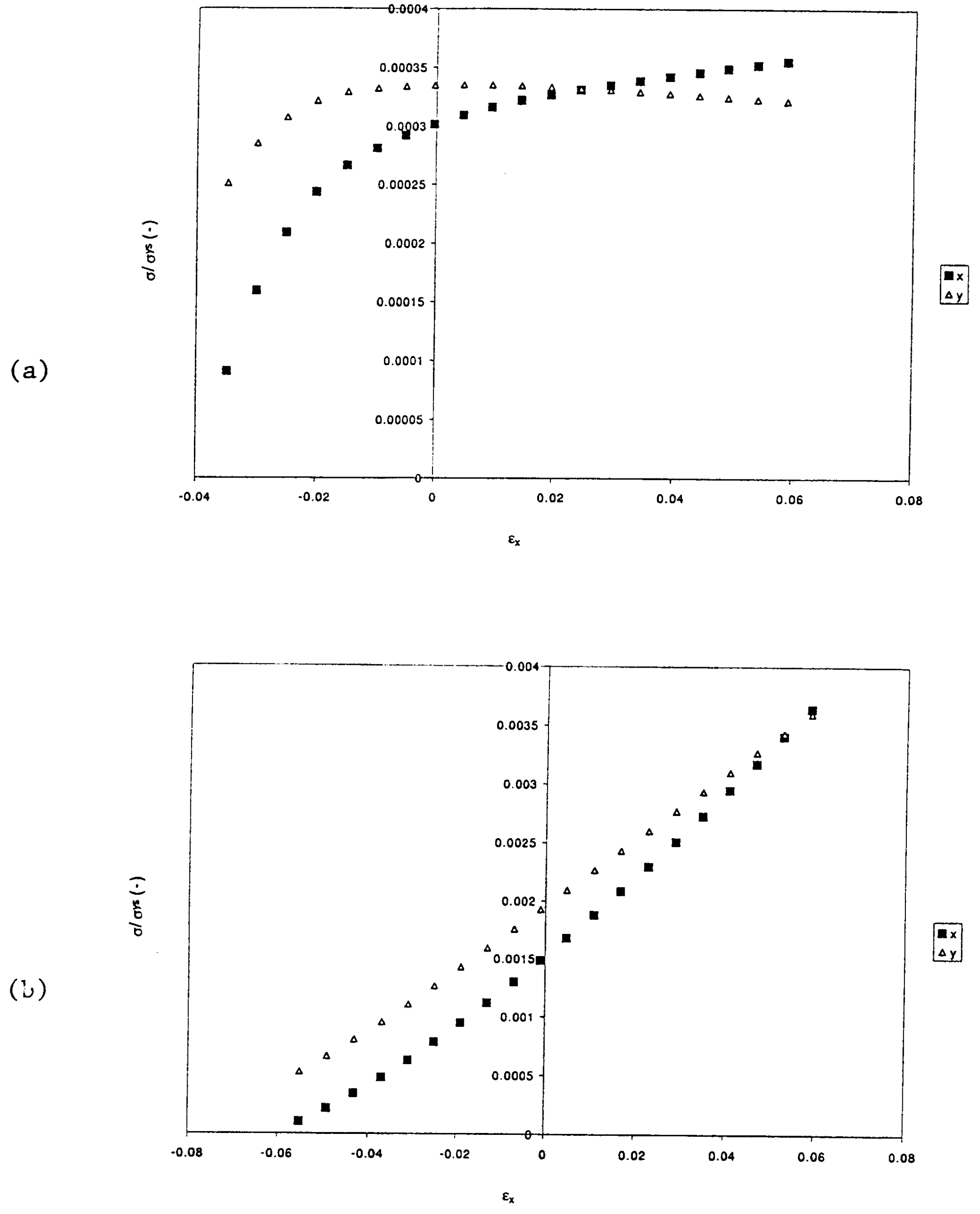

Figure 13: For the second step of biaxial (a) compression and (b) tension, σ_x/σ_{ys} and σ_y/σ_{ys} at each increment were plotted against ε_x, the strain in the direction of displacement in the second step. The ε_x axis begins at values less than zero due to the Poisson effect which allows the mesh to expand in the second direction during the displacement in the first step.

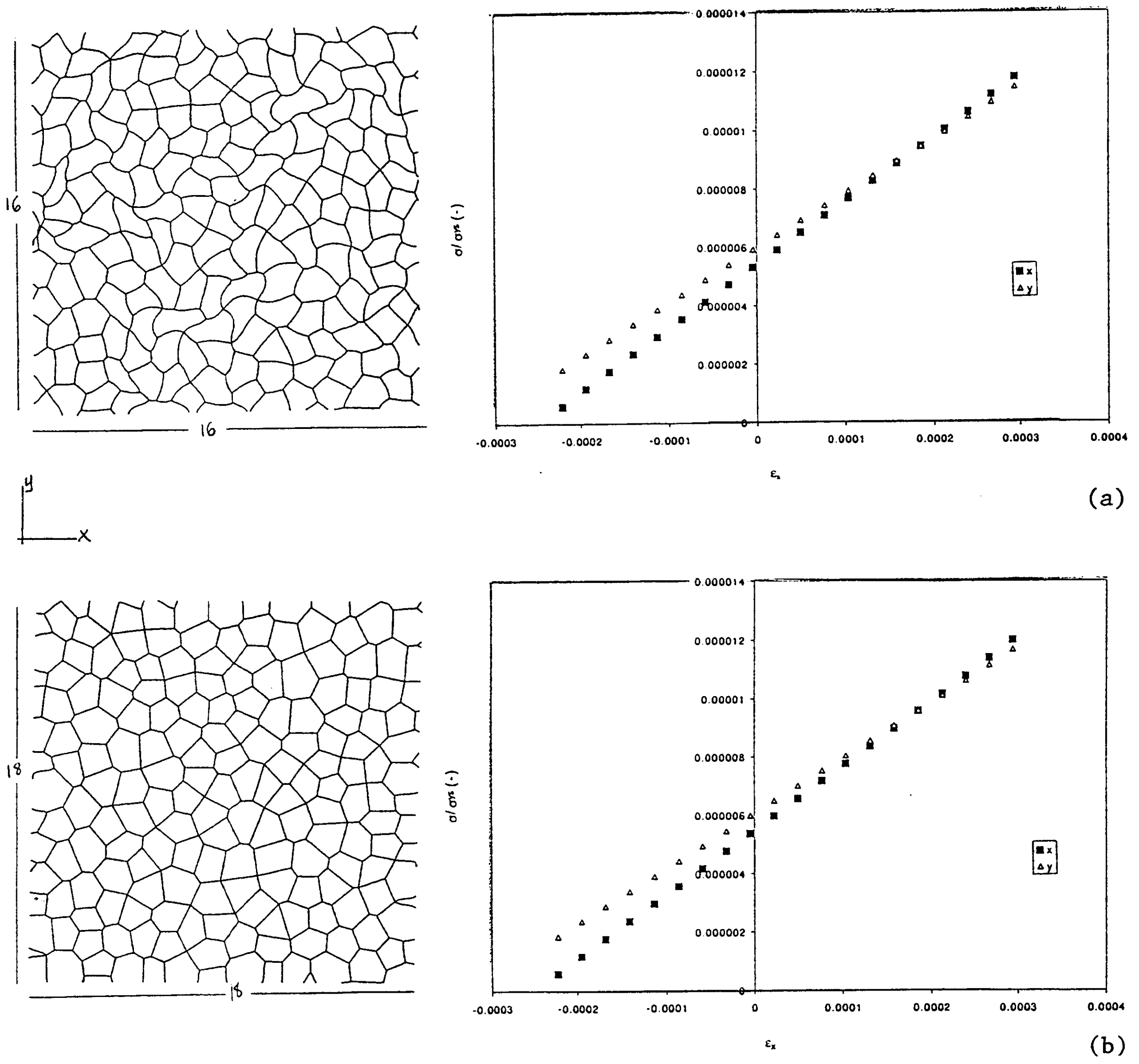

Figure 14: (a) Elastic cell walls bend when the Voronoi honeycomb is equibiaxially compressed from initial dimensions of 17x17 to 16x16. (b) The cell walls stretch to accommodate equibiaxial tension when the original mesh expands to 18x18. The relevant stress-strain data is presented for the second step of both loading scenarios.

Young's modulus for the Voronoi structure in the two directions was within the range of values reported in a previous study. Silva et al list (1995) elastic moduli for twenty isotropic Voronoi meshes with a relative density of 15%. They tested meshes with linear elastic cell walls given a Young's modulus of 1.0 and found the resulting elastic moduli to range from 0.433×10^{-2} to 0.583×10^{-2} (Silva et al, 1995). Their values compare with the values computed in this study of $E_x=4.42 \times 10^{-3}$ and $E_y= 4.13 \times 10^{-3}$.

The strength of the Voronoi honeycomb was 73% and 78% of the FEM solution for the strength of the hexagonal mesh in the x- and y-directions, respectively. These differences are consistent with a previous study that reported the mean strength of five Voronoi honeycombs with relative density of 0.15 to be 70% of the strength of the corresponding periodic hexagonal honeycomb (Silva and Gibson, 1997).

The failure envelope obtained for the Voronoi honeycomb was compared to the plastic yield surface predicted for regular hexagonal honeycombs in biaxial loading. Using the equation derived by Gibson et al (1989) to calculate the biaxial failure strength of a regular hexagonal honeycomb with $t/l=0.13$, the equibiaxial stress states are nearly seven times as great as the uniaxial failure strengths in both compression and tension.

The Voronoi honeycomb failure envelope varies considerably from the plastic yield surface shown above for the hexagonal honeycomb. Our envelope depicts a structure that is weaker than the periodic structure in both biaxial compression and in biaxial tension. Whereas the hexagonal mesh in equal biaxial loading could withstand nearly six times its uniaxial strength, the Voronoi mesh failed under equal biaxial loads less than two times its uniaxial compressive strength. The structure was also somewhat stronger in tension than in compression.

Both the relative weakness in biaxial loading of the Voronoi mesh compared to the hexagonal mesh and the relative weakness in compression versus tension for the Voronoi case alone can be explained by examining the contributions to failure due to stretching and bending of the cell walls. To achieve uniaxial deformation in a hexagonal honeycomb, the cell walls bend (Gibson et al, 1982; Papka and Kryakides, 1994; Warren and Kraynik, 1987). In the biaxial case, the bending moments can cancel so that the cell walls feel only axial forces (Gibson and Ashby, 1997). The cell walls stretch to achieve the extreme state of biaxial loading and are thus able to withstand much higher stresses than in uniaxial deformation (Gibson et al, 1989).

One might consider that the relative weakness of the Voronoi mesh in compression presents a different failure mechanism that dominates over plastic yielding. As shown in the plastic yield surface for a hexagonal honeycomb with t/l=0.1 (figure 1), elastic buckling of cell walls in compression will occur before the mesh reaches the plastic yield strength predicted by the theoretical expression. One should note that in our study, the relative density of the Voronoi honeycomb was taken at 15% (t/l=0.13) to ensure that plastic yielding would be the dominant failure mechanism.

For the Voronoi mesh, cell walls accommodated both uniaxial and biaxial stress states by a combination of stretching and bending. We computed element axial forces and section moments to characterize contributions to plastic failure made by stretching and bending, respectively, in the cell walls. We then plotted histograms to compare distributions of axial forces and section moments in equibiaxial tension and compression for the non-periodic structure.

The average axial force of the elements were nearly equal in both compression ($<S>_c=0.000113$) and tension ($<S>_t=0.000114$). The distribution varied only slightly for the two states, showing that the contributions to failure by stretching of cell walls were equally significant in both loading scenarios. In contrast to the axial force results, the element section moment analysis revealed that the average bending moment in compression ($<M>_c=4.24 \times 10^{-6}$) was nearly two times as much as the average section moment in tension ($<M>_t=2.26 \times 10^{-6}$). The histogram confirmed that in compression, more elements have higher bending moments than in tension.

Large deformation analysis of the Voronoi mesh with linear elastic cell walls clearly depicted the dominant failure mechanism for the two loading states. In compression, the walls appear uniformly bent, whereas in tension, there is no apparent bending in the cell walls. Figure 14 shows the walls stretching in their axial direction to achieve the state of equibiaxial tension.

A comparison of the bulk moduli of hexagonal and Voronoi honeycomb supports the bending and stretching conclusion. Equation 7 was evaluated to determine the theoretical bulk modulus for a hexagonal honeycomb, $K_{hex}=0.037$. The bulk modulus for the Voronoi mesh was similarly computed using FEM results for the mesh with linear elastic cell walls. The Voronoi mesh exhibited a much lower modulus, $K_{Vor}=0.020$. Bulk modulus physically represents the extent to which a bulk material deforms under uniform pressure. The bulk modulus values reported in this study are consistent with the failure envelope which depicts a material weaker in the extreme biaxial stress states than the corresponding periodic structure.

In practice, rotational constraints at the edge nodes are unrealistic compared to physical specimens of foams which would not be constrained at the edges. An accurate prediction of experimental results for a three-dimensional specimen in hydrostatic compression would fall somewhere between the constrained and unconstrained models. Plastic collapse strength is sensitive to small defects so the experimental results may be systematically less than theory or computational results would predict (Gibson and Ashby, 1997). Our computational results predict failure in equibiaxial compression to occur at biaxial stresses equal to 1-1.5 times the uniaxial material yield strength. Failure in equibiaxial tension takes place at approximately two times the uniaxial failure strength.

This study has several strengths. The computational approach enabled us to determine the failure mechanism in the biaxial loading state by determining the stress states in each element. The dimensionless results are highly reproducible and can be qualitatively applied to predict results for plastic yield surfaces of cellular solids having 15% relative density.

Certain limitations to this study should be noted. The failure envelope described here represents only one specific arrangement of cells. Increasing the number of non-periodic arrangements would improve the accuracy of the predicted yield surface. The study could also be extended to determine how properties like bulk modulus and failure mechanisms vary with changing relative density. Finally, the finite element model might be improved by using elements of the same length as opposed to dividing each cell wall into equal numbers of segments.

3.5 Conclusions

In this chapter we computed the failure envelope of a two-dimensional non-periodic cellular solid under biaxial loading. FEA results show that the material has a lower plastic failure strength in both biaxial tension and compression compared to a regular hexagonal honeycomb of the same relative density. The non-periodic honeycomb exhibited greater strength in equibiaxial tension than in equibiaxial compression due to larger bending moments in the elements for external compression loading. These results shed light on the mechanical behavior of random foams under hydrostatic loading.

3.6 References

Gibson LJ and Ashby MF. Cellular Solids: Structure & Properties. Pergamon Press, Oxford, 1997.

Gibson LJ, Ashby MF, Schajer GS and Robertson CI. *Proc. R. Soc. Lond.* 1982; **A382**: 25.

Gibson LJ, Ashby MF, Zhang J, and Triantafillou TC. Failure Surfaces for cellular materials under multiaxial loads—I. Modelling. *Int. J. Mech. Sci.* 1989; **31**: 635-663.

Papka SD and Kyriakides S. In-plane compressive response and crushing of honeycomb. *Journal of Mechanics and Physics of Solids,* 1994; **42**: 1499-1532.

Silva MJ. Ph.D. thesis. Department of Mechanical Engineering, Massachusetts Institute of Technology, Cambridge, 1996.

Silva MJ and Gibson LJ. The effects of non-periodic microstructure and defects on the compressive strength of two-dimensional cellular solids. *Int. J. Mech. Sci.,* 1997; **39**: 549-563.

Silva MJ, Gibson LJ and Hayes WC. The effects of non-periodic microstructure on the elastic properties of two-dimensional cellular solids. *Int. J. Mech. Sci.* 1995; **37**: 1161-77.

Warren WE and Kraynik AM. Foam Mechanics: the linear elastic response of two-dimensional spatially periodic cellular materials. *Mechanics of Materials,* 1987; **6**: 27-37.

4 Fatigue of trabecular bone

4.1 Background

All bones contain trabecular (also termed spongy, cancellous, or marrow bone) and cortical (or compact) bone (Schiller, 1994). Trabecular bone (figure 1) appears as a porous network of connecting rods or plates (Gibson, 1985) and can be found at the ends of long bones within the medullary canal (Schiller, 1994). As a consequence of aging and osteoporosis, the horizontal and vertical struts in the trabecular lattice thin and even disappear, resulting in the loss of bone strength. These age-related effects on the structure and mechanical behavior of trabecular bone are well documented (Ding, 1999; Mosekilde, 1988, 1989; Snyder, 1993).

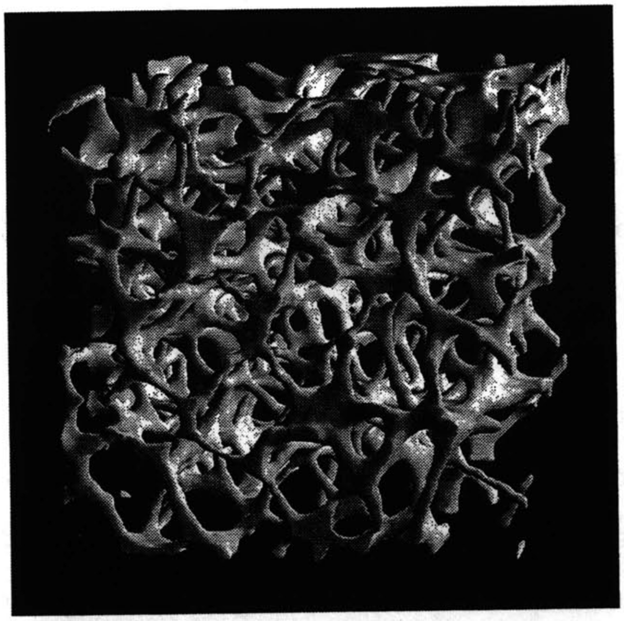

Figure 1: Trabecular bone is a partly open, partly closed cellular material. (Image courtesy of Ralph Mueller.)

Early models of trabecular bone focused on the response to monotonic loads using a variety of structural representations. Beaupre and Hayes used a three dimensional unit cell for a porous model to study the modulus as a function of density (1985). Jensen et al used a three dimensional cubic lattice with struts of different cross-secitional areas to model the effects of aging (1990). Silva and Gibson randomly removed struts from a two-dimensional hexagonal honeycomb to simulate the effects of trabecular thinning and disappearance due to aging (1997).

Microdamage accumulation has been proposed as a factor that contributes to skeletal fragility with age, especially for older women (Burr et al, 1997). There is strong evidence of microcrack growth due to fatigue in cortical bone, and recent studies have begun to explore these phenomena in trabecular bone (Burr et al, 1995; Huja et al, 1999; Reilly et al, 1999; Schaffler et al, 1996; Vashishth et al, 1996; Vashishth et al, 1997; Vashishth, 1999). Several studies describe mechanical behavior of bone in dynamic loading conditions as well. Michel and Bowman reported cycle-dependent and time-dependent response to repeated loading in trabecular bone and suggest that creep-fatigue interaction contributes to failure (Bowman et al, 1994; Bowman et al, 1998; Michel et al, 1993). A similar interaction was found in earlier experimental studies of cortical bone (Caler and Carter 1989; Carter and Caler, 1983).

Finite element models and analytical methods have been used to characterize and distinguish between fatigue and creep contributions to failure in trabecular bone. Guo used a two dimensional hexagonal honeycomb with a beta distribution of crack lengths to model the effects of fatigue due to microcrack growth in trabecular bone (1994). This study contrasted the effects of fatigue and creep and suggested the presence of a creep-fatigue interaction as has been shown for cortical bone.

In this study, we propose a new model to characterize effects of fatigue and creep in trabecular bone. We believe that the rod-like structure of trabecular bone can be better represented by a three dimensional Voronoi network. Like the two dimensional Voronoi honeycomb described in chapter 3, Voronoi solids in three dimensions have been used to model the mechanical behavior of open and closed cell foams (Kraynik, 1997; Schulmeister, 1997; van der Burg, 1997). A Voronoi solid (figure 2) has straight edges and flat surfaces with the proper connectivity of a soap froth. The open Voronoi network mimics the structure of trabecular bone which appears mostly rod-like in the later stages of life.

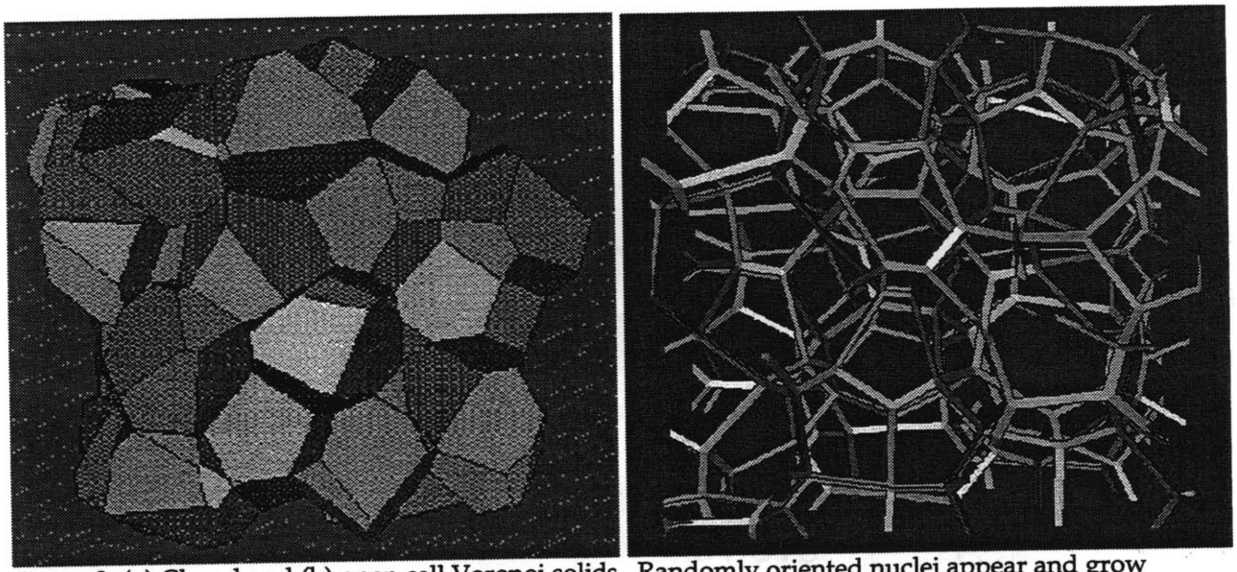

Figure 2: (a) Closed and (b) open cell Voronoi solids. Randomly oriented nuclei appear and grow spherically at the same rate; growth ceases when one cell contacts a neighboring cell.

In this chapter we build on concepts explored in previous chapters and apply the results to a physically meaningful problem. We extend the Voronoi honeycomb to three dimensions and use the finite element method to study the effects of cyclic compression on a unit cell of a low density open cellular solid. Finally, we extrapolate these results to apply them to a higher density cellular solid and compare our findings to studies of creep and fatigue contributions to failure in trabecular bone.

4.2 Methods

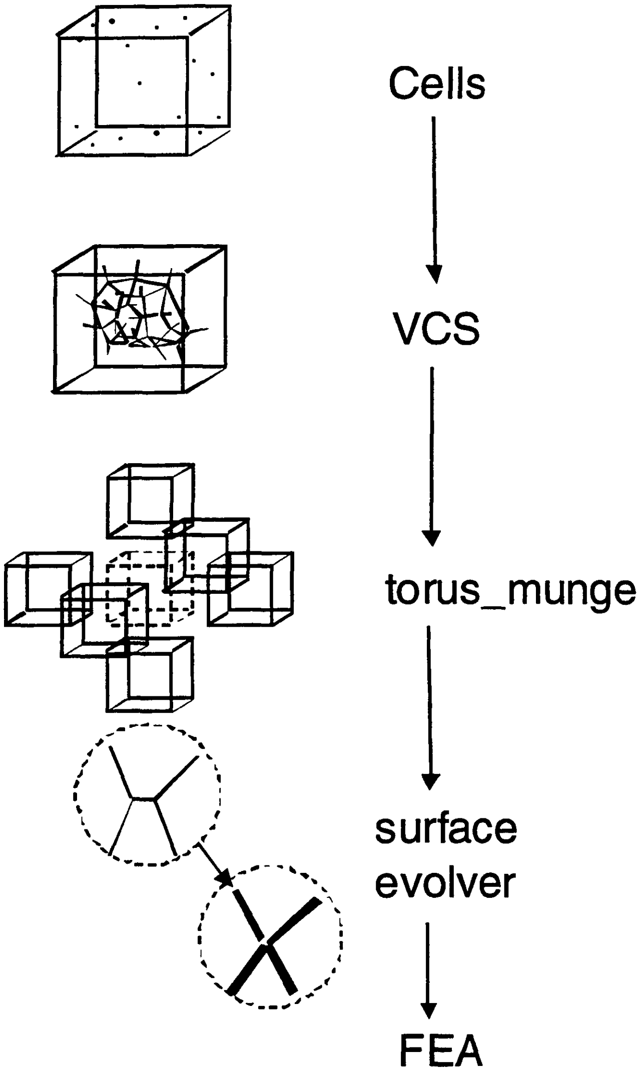

Figure 3: Schematic overview of mesh generation.

Mesh Generation

Three-dimensional Voronoi networks were created using software from the University of Minnesota Geometry Center (UMNGC) and Sandia National Laboratories (SNL) (figure 3) based on the method of Kraynik (1997). *Cells* (Sullivan, 1997) was used to generate random seeds for a unit cell of a Voronoi network.

Different random seeds were used to produce five Voronoi models, each with twenty-seven cells. Cell seeds were placed to achieve cell radii less than or equal to 77% of a cell's radius in an equivalent face centered cubic (fcc) crystal lattice for a 3x3x3 mm^3 unit cell (figure 4).

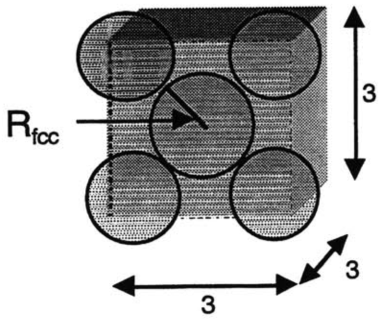

Figure 4: Spacing was set so that the radius of each cell in the Voronoi network was greater than or equal to 77% of R_{fcc}, the radius of an atom in a face centered cubic unit cell, shown in the figure above.

The program *VCS* (Sullivan, 1988) was used to create and connect the vertices of the Voronoi network. *Torus_munge* (Sullivan, 1988) was used to make the structures spatially periodic. A spatially periodic unit cell repeats infinitely in space, thus eliminating edge effects from the mechanical analysis.

The UMNGC *Surface Evolver* (Brakke, 1998) was used in conjunction with a number of software programs from SNL (Kraynik et al, 1998) to remove short edges and to produce an input file for the finite element modeling software, ABAQUS (HKS, 1997). It has been shown that removal of short struts does not influence the accuracy of results (Schulmeister, 1997). The constant cross-sectional area of the struts was computed by dividing the product of the relative density and unit cell volume by the sum of the lengths of all struts. Because this approximation greatly overestimates the volume of material contained in the joints at high relative densities, our structures were limited to relative densities, ρ^*/ρ_s less than or equal to 0.1%. Also, a low relative density ensures that beam elements adequately model the struts since the resulting element aspect ratio would satisfy beam theory. Based on these considerations, relative density was set at ρ^*/ρ_s=0.1%.

The five final structures used in this study had three-noded three-dimensional beams (ABAQUS type B31) with uniform circular cross-sections (figure 5). The strut material had properties of human trabecular bone: Young's modulus E_s=17.2x10^3 MPa (Rho et al, 1998) and Poisson's ratio ν_s=0.3. Each model represented a 3x3x3 mm^3 unit cell defined by three basis vectors in the input file:
<3 0 0> , <0 3 0>, and <0 0 3>.

Convergence study

A convergence study was conducted on a representative model to identify an adequate number of elements per strut and to determine the appropriate amount of strain per increment. Input files were created for structures having struts divided into two to eight elements, on average. After a uniaxial compression to ε=1.0%, reaction forces were reported at each basis vector node and true stress was computed. True stress values were plotted as a function of degrees of freedom and as a function of average number of elements per cell wall. For a strain of 1.0%, the stress values converged to within 0.23% of the true solution when struts were modeled using seven elements (figure 6). A typical mesh consisted of approximately 2200 elements and 2500 nodes. By varying the amount of strain per increment in a one step uniaxial compression (ε=1.0%) of a model with an average of seven elements per strut, we found that 0.001 strain, or ε=0.1%, per increment gave stress values which converged to within 0.16% of the exact solution.

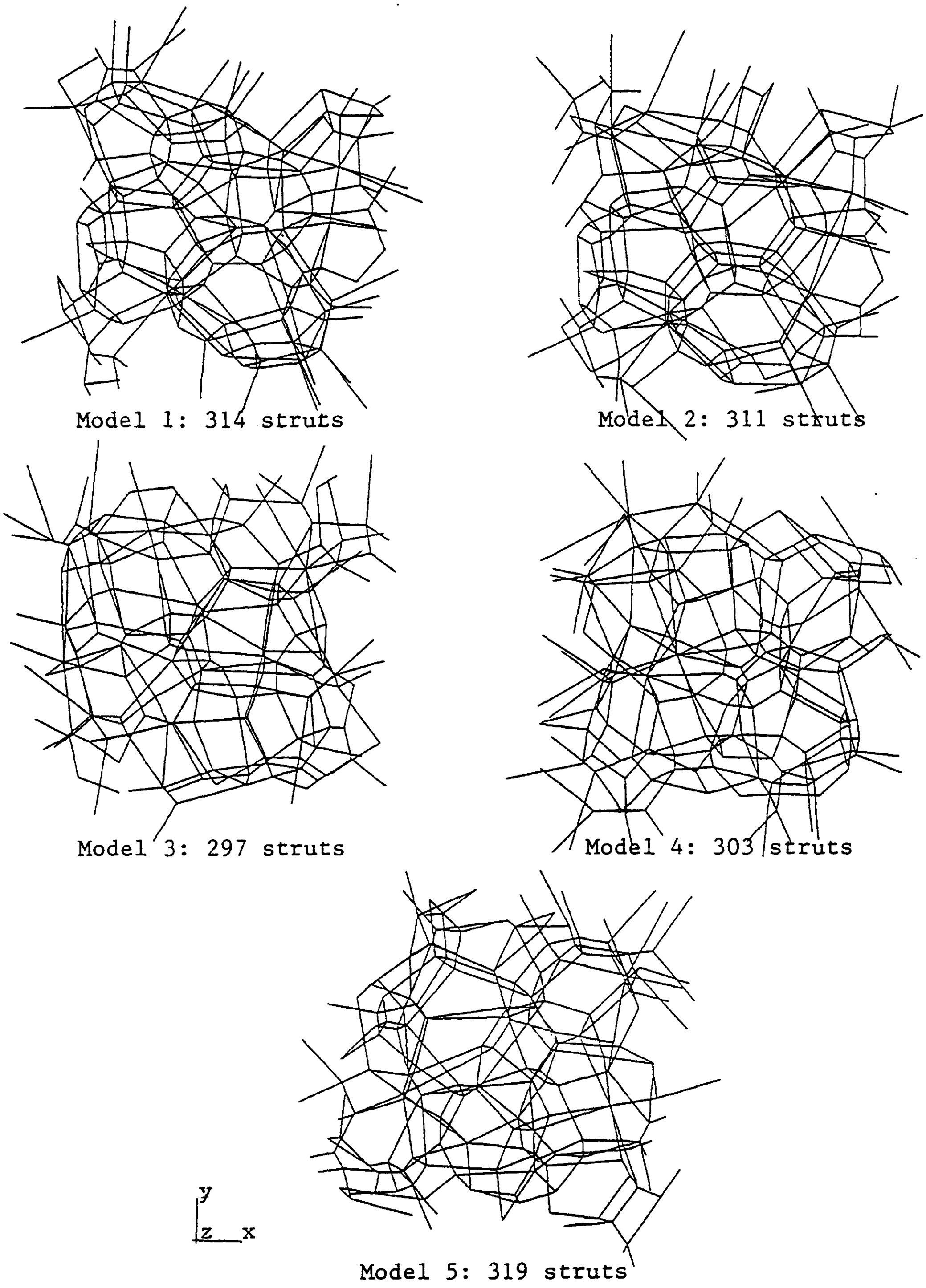

Figure 5: Five models of Voronoi networks. The number of struts in each model is given next to each model. Each model occupies a 3x3x3 mm^3 unit cell with three orthogonal unit vectors: <3 0 0>, <0 3 0>, and <0 0 3>.

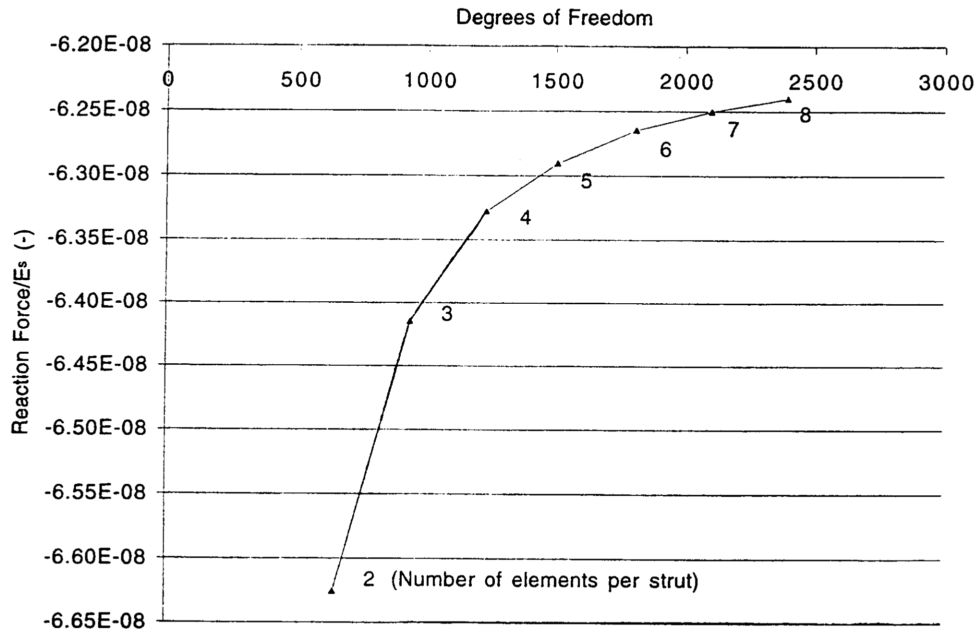

Figure 6: Reaction force values converged when struts were modeled using seven elements.

Finite element analysis

Finite element analysis (FEA) was performed for each model. Each structure was loaded by boundary condition displacement applied at the node of the third basis vector <0 0 3> in the z-direction. Five loading values of $\Delta\sigma/E_0$ were chosen: 1%, 3%, 5%, 7%, and 10%. For each model, E_0 was calculated by dividing the stress, σ by the strain, ε for a model in uniaxial compression. In each case, E_0 was computed at 0.1% strain.

A separate analysis was performed to determine the displacement and number of increments required to achieve the $\Delta\sigma/E_0$ value. Using data on reaction forces and displacements at the nodes, stress and strain were calculated at each increment (0.1% strain) of an analysis in which the structure was compressed to a strain large enough to achieve the specified $\Delta\sigma/E_0$ value. We then identified the strain and exact number of increments corresponding to a loading level just less than or equal to the $\Delta\sigma/E_0$ required for the analysis. In all cases, $\Delta\sigma/E_0$ was within 0.04% of the specified value.

Once the appropriate boundary condition displacement had been determined, FEA was used to compute and report the axial reaction forces (SF1), section bending moments (SM1, SM2), and section twisting moment (SM3) at the centroid of each element (figure 7). These values were used in the fatigue calculations described below.

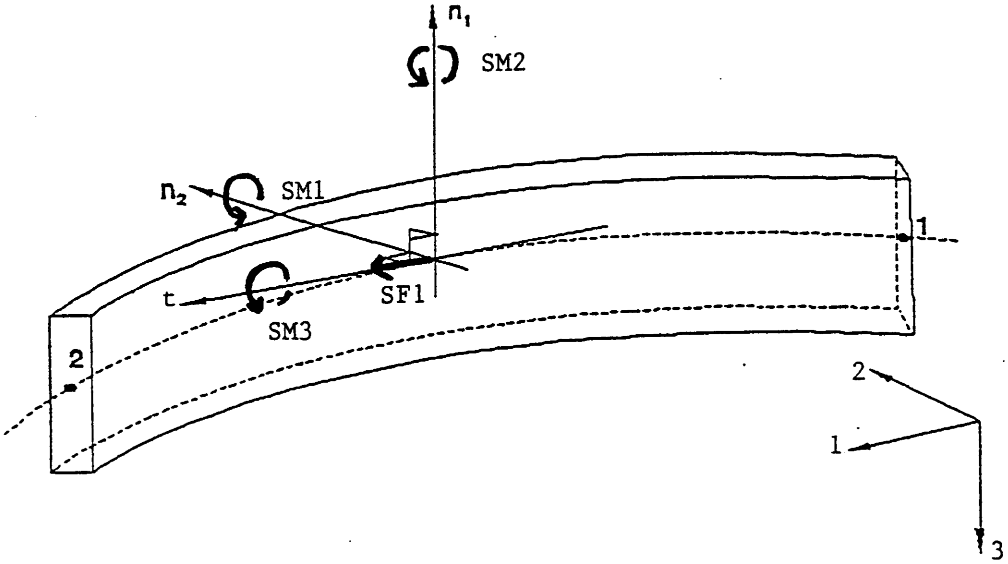

Figure 7: Geometry of beam and stress values. Finite element modeling software was used to compute the axial force SF1, bending moments SM1 and SM2, and twisting moment SM3 with respect to the local coordinate system of each beam element.

Fatigue calculations

Based on studies of damage accumulation and fatigue in bovine trabecular bone (Lee, 1997; Arthur, 1999) a semi-elliptical surface crack was selected for placement in 10% of the trabeculae in each model. Cracks were assumed to be in the worst configuration, i.e. on the surface experiencing the greatest bending moment. The initial crack length a_0 was set to 1/4 of the diameter of the trabecular cross section.

The strain energy release rate, G, was used to combine stress intensity factors for the three modes of loading (Anderson, 1995):

$$G = \frac{K_I^2}{E} + \frac{K_{II}^2}{E} + \frac{K_{III}^2}{2\mu}, \tag{1}$$

where K_I, K_{II}, and K_{III} are the stress intensity factors for opening, sliding, and tearing modes, respectively. The shear modulus, μ, is given as

$$\mu = \frac{E}{2(1+\nu)}, \tag{2}$$

where ν is Poisson's ratio.

Using the strain energy release rate, we derived an effective stress intensity factor for the opening mode, $K_{I,eff}$, by combining these terms to characterize the total effects of the three loading modes:

$$G = \frac{K_I^2}{E}$$

$$K_{I,eff} = \sqrt{GE}$$

$$K_{I,eff} = \sqrt{K_I^2 + K_{II}^2 + K_{III}^2(1+\nu)}. \tag{3}$$

Stress intensity factors for a surface crack in a three-dimensional cylindrical beam were obtained from several previous studies of stress intensity factors for various semi-elliptical surface crack geometries (Levan and Royer, 1993; Murakami, 1987; Rooke and Cartwright, 1976).

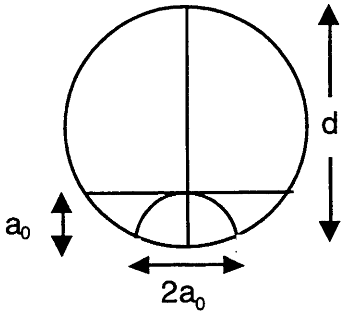

Figure 8: Geometry of semi-circular surface crack on trabecular cross-section. The initial crack length a_0 at the crack front was set to 1/4 of the trabecular diameter, d.

Based on previous studies of microcracks in trabecular bone (Arthur, 1998; Lee, 1997; Taylor and Lee, 1998) we selected a semi-circular crack with an initial crack length, a_0, equal to 1/4 of the trabecula cross-section diameter, d (figure 8). Levan and Royer give normalized stress intensity factors $K/(\sigma(\pi b)^{0.5})$ as a function of relative crack depth a/R for various crack shapes (figures 9 and 10) Murakami reports calculated values of the normalized stress intensity factors for our geometry and initial crack length, a_0=0.25d as 0.758 for a shaft under tension and 0.513 for a shaft under bending (1987).

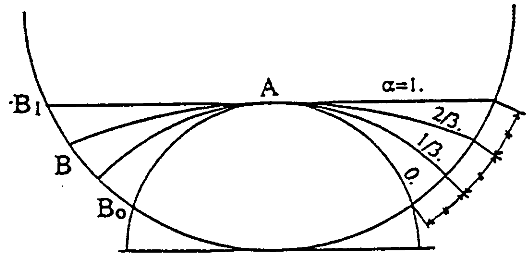

Figure 9: Crack shapes for the surface cracks defined by parameter α. (from Levan and Royer, 1993)

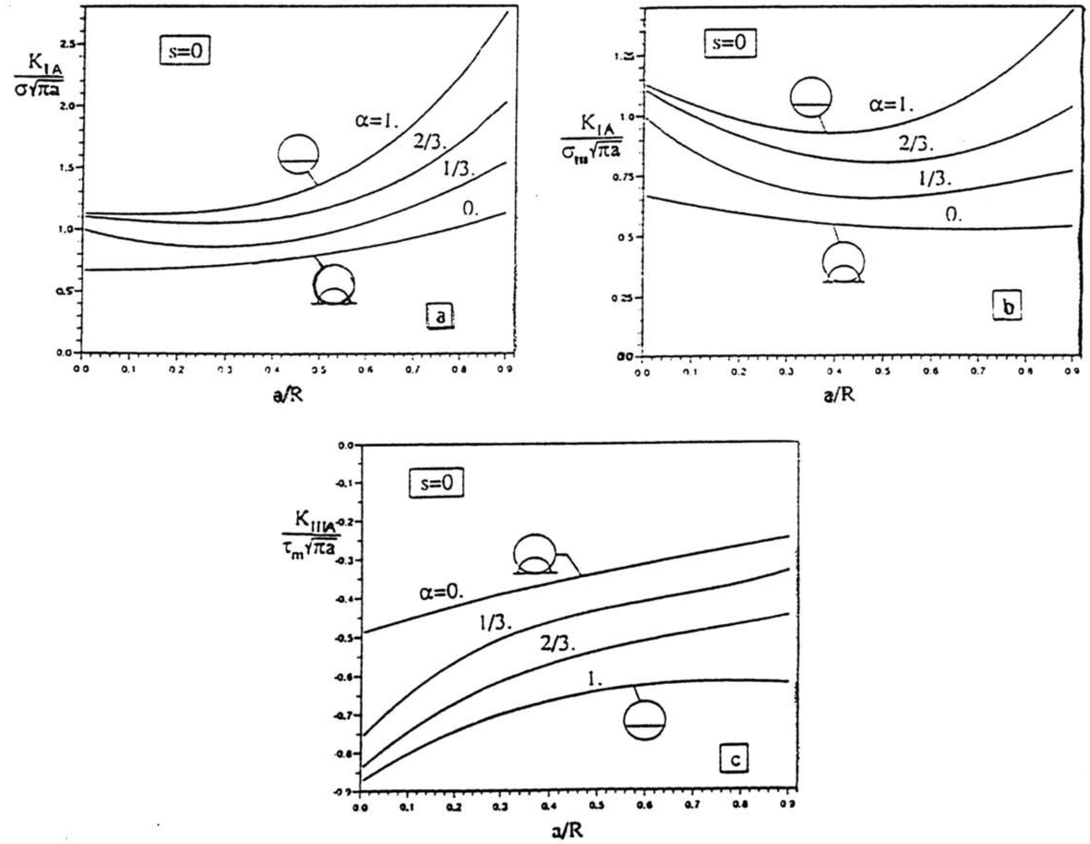

Figure 10: Normalized stress intensity factors versus the relative crack depth. (a) Tension. (b) Bending. (c) Torsion. (from Levan and Royer, 1993)

Based on these studies, our geometry corresponded to the following stress analysis factors:

$$K_I^B = 0.513\sigma_b\sqrt{\pi a} \tag{4}$$

$$K_I^T = 0.758\sigma_t\sqrt{\pi a} \tag{5}$$

$$K_I = K_I^B + K_I^T \tag{6}$$

$$K_{III} = -0.325\tau_m\sqrt{\pi a} \tag{7}$$

where K_I^T and K_I^B are the stress analysis factors for tension and bending, respectively. The two factors are combined to obtain the stress analysis factor for the opening mode. (Note that there is no sliding mode for this geometry; therefore, $K_{II}=0$.) The bending moment σ_b, axial stress σ_t, and twisting moment τ_m were calculated for each element using the data obtained from FEA (Crandall et al, 1978):

$$\sigma_b = \frac{4\sqrt{SM_1^2 + SM_2^2}}{\pi r^3} \tag{8}$$

$$\sigma_t = \frac{SF_1}{\pi r^2} \tag{9}$$

$$\tau_m = \frac{2SM_3}{\pi r^3} \tag{10}$$

where r is the radius of the trabecula cross-section. By combining the two reported section moments SM_1 and SM_2, we assumed that each crack was placed in the worst possible configuration for the element, i.e. on the portion of the surface which experiences the highest bending force.

Combining equations 3-10, we obtained the following expression for $\Delta K_{I,eff}$:

$$\Delta K_{I,eff} = \sqrt{((A+B)^2 + C)}\sqrt{a}, \tag{11}$$

where

$$A = \frac{(0.513 \times 4)}{r^3}\sqrt{\frac{SM_1^2 + SM_2^2}{\pi}},$$

$$B = \frac{(0.758)SF_1}{r^2\sqrt{\pi}}, \text{ and}$$

$$C = \left(\frac{(-0.325 \times 2)SM_3}{r^3}\right)^2\left(\frac{1+v}{\pi}\right).$$

Details of the derivation are given in the Appendix.

The microcracks were assumed to grow under cyclic loading by the Paris law (Paris and Erdogan, 1963):

$$\frac{da}{dN} = C_p(\Delta K)^m \tag{12}$$

where da/dN (10^{-6} m cycle^{-1}) is the crack growth rate and ΔK (MNm$^{-1.5}$) is the opening mode stress intensity factor range for cyclic loading. Based on the only existing data for bovine cortical bone, the constant C and exponent m of the Paris law were taken as 0.013 and 4.5 (Wright and Hayes, 1976). After integrating and accounting for variations in units, we obtained the following expression:

$$a_f = \exp\left\{\left(\frac{2}{2-m}\right)\ln\left[a_0^{\frac{2-m}{2}} + \frac{2}{2-m}C_p\left((A+B)^2 + C\right)^{\frac{m}{2}} \cdot 10^{-1.5m-3} \cdot N\right]\right\}, \tag{13}$$

where a_f (m^{-3}) is the final crack length taken at the crack front after N cycles.

Based on equation 13 the element force and moment data obtained by FEA were used to compute the total number of cycles required for an element to fail, N. We assumed that the element fractured when the final crack length exceeded 3/4 of the diameter of the trabecula cross section. After an element failed, the element number and number of cycles to failure were recorded. The element was removed from the model, and the new mesh was analyzed using the FEA procedure described above. Young's modulus was calculated for the new mesh, the number of increments or strain required to achieve the specified Δσ/E value was determined, and the element forces and moments were calculated again. This process was repeated iteratively until Young's modulus for the model had decreased by at least 15% (figure 11). The number of cycles required for the 15% reduction was then recorded as the number of cycles to failure, N_f.

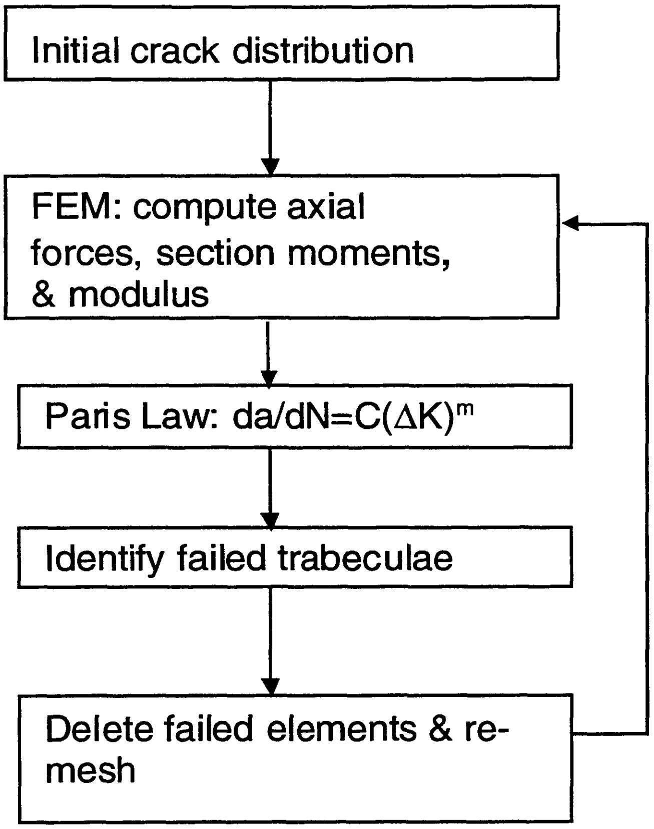

Figure 11: Summary of FEA and fatigue calculations.

Extending the model to trabecular bone

We developed a dimensional argument to extend the Voronoi model results to trabecular bone. Consider a single trabecular strut subject to an external load (figure 12).

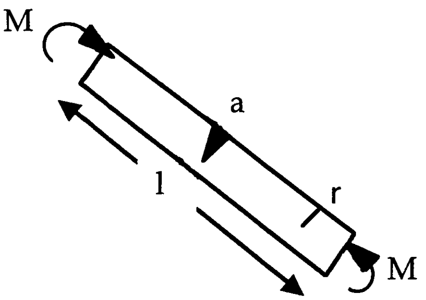

Figure 12: External bending moment M applied to single trabecular strut with radius r, length l, and crack length a.

When an external stress is applied, the strut will initially deform by bending. The stress will be related to the bending moment M by

$$\sigma \propto \frac{My}{I}, \tag{14}$$

where I is the moment of inertia. This expression relates to the external stress σ^* by

$$\frac{My}{I} = \frac{\sigma^* l^3 r}{r^4}, \tag{15}$$

so that equation 14 becomes

$$\sigma \propto \sigma^* \left(\frac{l}{r}\right)^3. \tag{16}$$

We can substitute the relative density into equation 16 using the following relation:

$$\left(\frac{\rho^*}{\rho_s}\right) \propto \left(\frac{r}{l}\right)^2. \tag{17}$$

The stress intensity factor ΔK describing the growth of the crack is given as

$$\Delta K \propto \sigma\sqrt{\pi a}. \tag{18}$$

We use equations 16-18 to derive a relationship between the stress intensity factor and the relative density:

$$\Delta K \propto \sigma^* \left(\frac{\rho^*}{\rho_s}\right)^{-\frac{3}{2}} \sqrt{\pi a}. \tag{19}$$

Note that we can convert the applied stress to the normalized fatigue stress range value using the following expression:

$$\sigma^* \propto \left(\frac{\rho^*}{\rho_s}\right)^2 E_s \frac{\Delta\sigma}{E} \tag{20}$$

(Gibson, 1999).

The Paris law for crack growth (equation 12) becomes

$$\frac{da}{dN} = C_{Vor}\left[\frac{\Delta\sigma}{E} E_s \left(\frac{\rho^*}{\rho_s}\right)^{\frac{1}{2}} \sqrt{\pi a}\right]^m \tag{21}$$

where C_{Vor} is a scaling constant which incorporates the Paris constant and must be calculated from the Voronoi model results. Note that our analysis ignores the axial and twisting components since A, the bending component of $\Delta K_{I,eff}$ (equation 11) was the dominant term for most of the fractured members, e.g. A/B~40, A/C~40. We integrated the equation and computed C_{Vor} for each of the five models at each of the five normalized stress range values. We then used the constants to calculate the number of cycles required for the five models to fail at each stress range, assuming a new relative density ρ^*/ρ_s=0.30. Finally, we compared these scaled results to the experimental and computational results reported in previous studies on trabecular bone.

4.3 Results

Young's modulus for each of the intact structures is given in table 1. Each mesh required five to nine members to fracture for a 15% reduction in Young's modulus for the structure (figure 13). Young's modulus was recalculated each time an element was removed. The reduction in Young's modulus can be seen in the stress-strain curves in figure 14. Data was successfully obtained for all models at all stress levels except for the fifth model at the 10% fatigue stress. The finite element analysis results did not converge, and results were not included for this model at the highest fatigue stress.

Table 1: Data for intact structures

Model Number	E_0 (MPa)	Number of elements	Number of nodes
1	1.23×10^{-2}	2196	2109
2	1.37×10^{-2}	2176	2087
3	1.49×10^{-2}	2081	1997
4	1.51×10^{-2}	2121	2033
5	1.46×10^{-2}	2236	2141

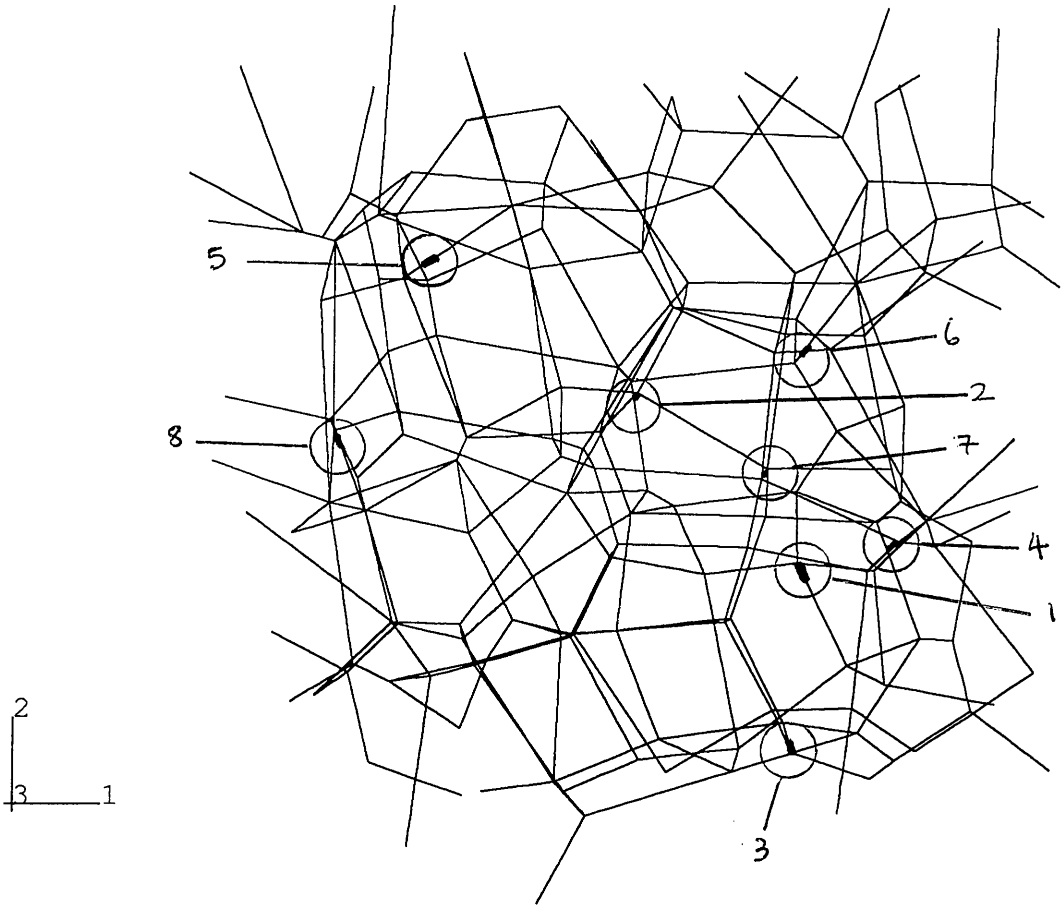

Figure 13: This intact model had 2081 elements. Fractured elements, shown in red, are numbered in the order in which they fractured and were removed.

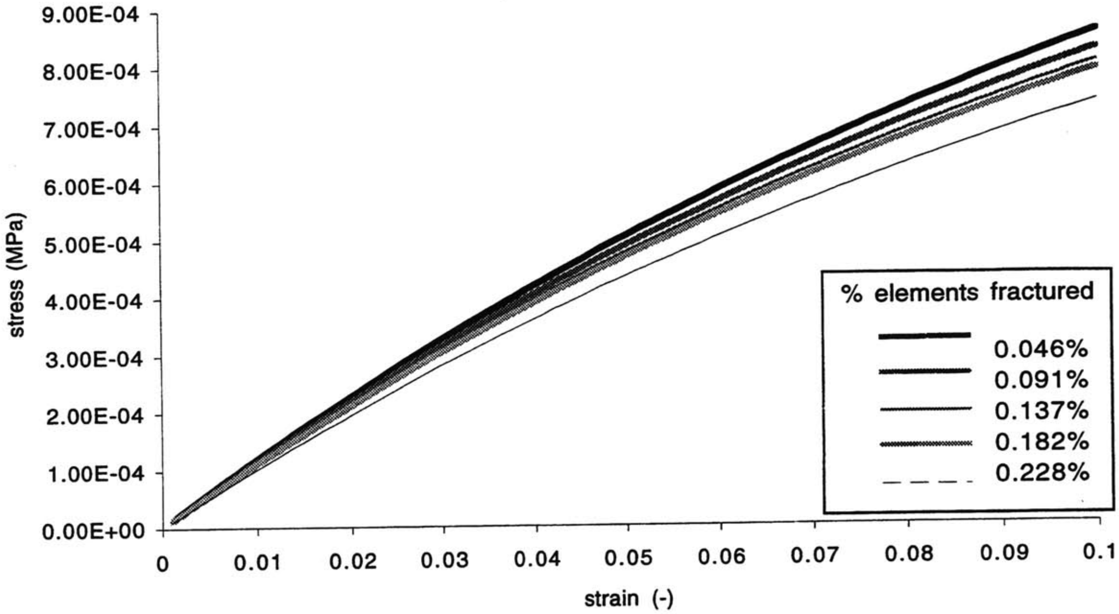

Figure 14: Stress-strain curves show reduction in Young's modulus. After an element fractured, the structure's stress-strain curve was plotted and Young's modulus was calculated for the new mesh.

For each model, the fatigue stress values $\Delta\sigma/E_0$ and the fraction of elements which had failed was plotted against the total number of cycles to failure. As the loading value increased, fewer cycles were required to achieve the 15% reduction in Young's modulus (figure 15).

The relative modulus E/E_0 was also plotted against the number of cycles for each model. For some models, the elements failed in the same order for each loading value (figure 16a); for others, different elements failed or the same elements failed but in a slightly different order (figure 16b). The number of cycles to failure for each model at a given load were averaged and plotted against the fatigue stress values on a log-log plot (figure 17). These values are given in Table 2 below. There was a strong ($r^2 = 0.976$) power law relationship between the number of cycles-to-failure N_f and the applied normalized stress range $\Delta\sigma/E$:

$$\log N_f = -0.4900 - 8.651 \cdot \log\left(\frac{\Delta\sigma}{E}\right) \tag{22}$$

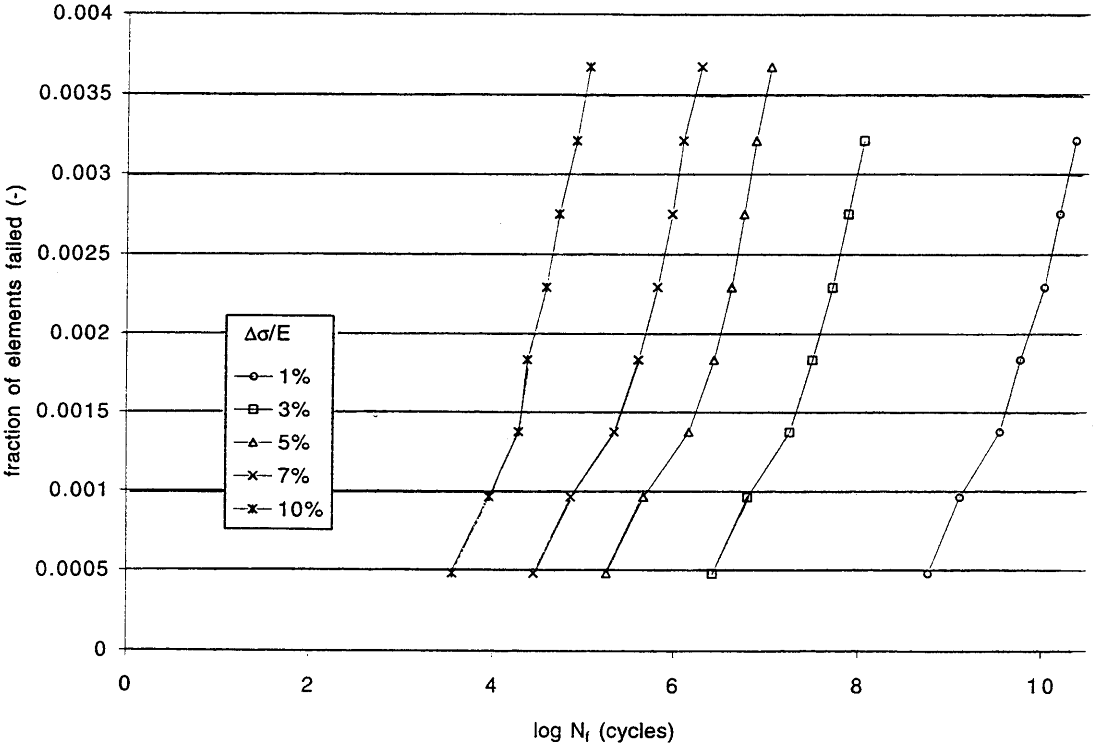

Figure 15: Fraction of fractured elements was plotted against number of fatigue cycles at each $\Delta\sigma/E_0$ value for a model. For lower $\Delta\sigma/E_0$ values, more cycles were required to substantially reduce the intact structure's Young's modulus.

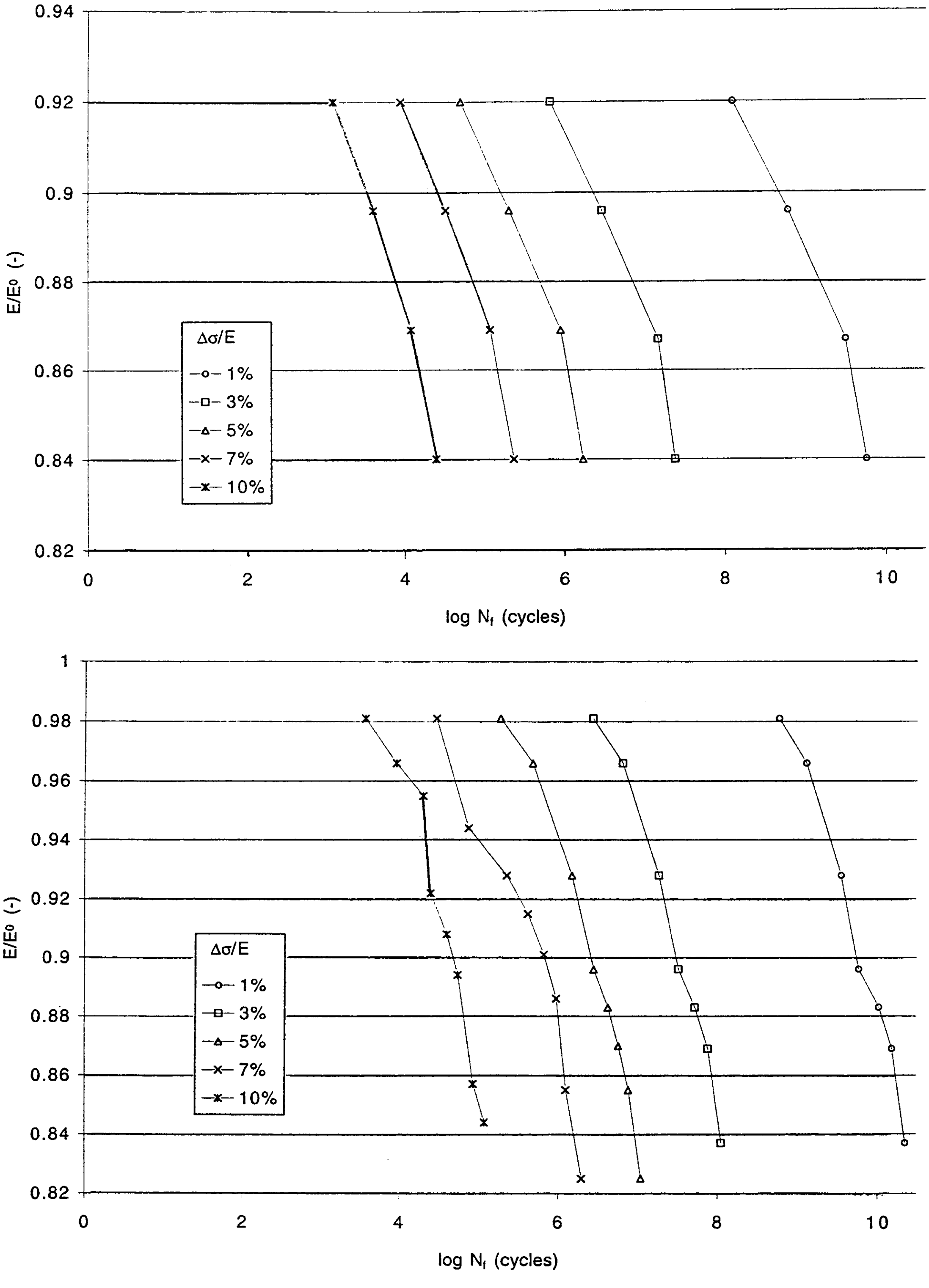

Figure 16: Relative modulus E/E_0 was plotted against number of fatigue cycles at each $\Delta\sigma/E_0$ value for a model. The parallel curves (a) depicts a model whose elements fractured in the same sequence at each fatigue stress. Figure 16b represents a model which had different elements fail or had the same elements fail in a different sequence at each stress level.

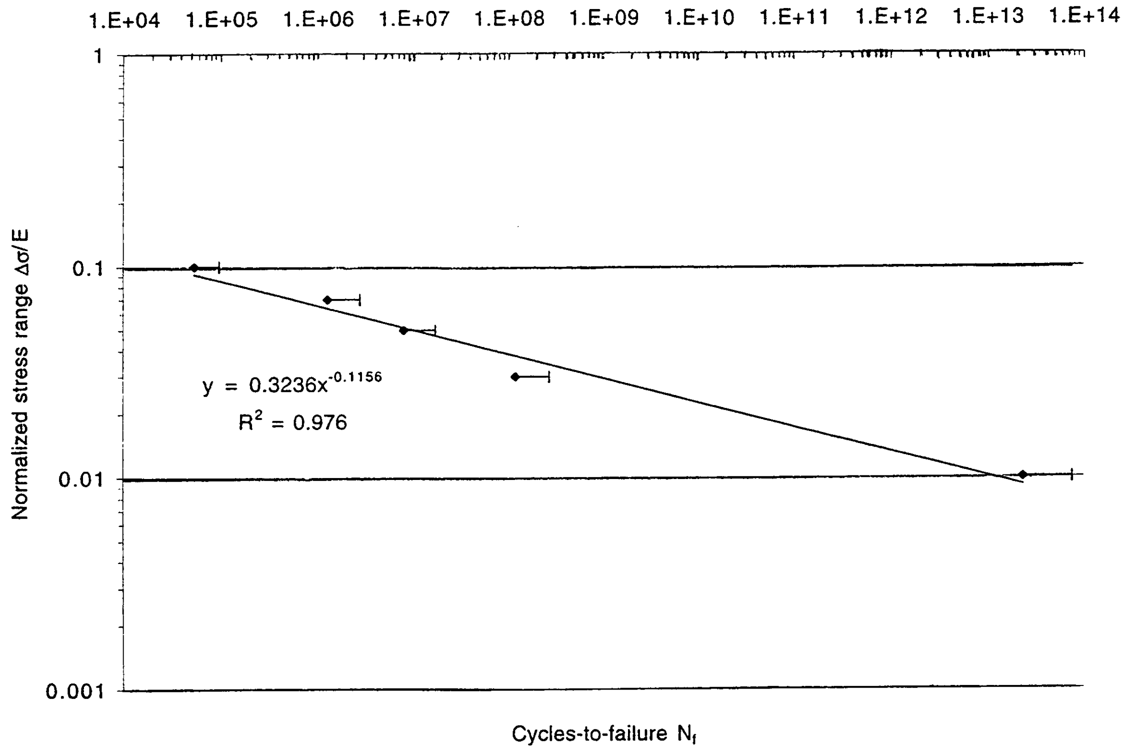

Figure 17: Summary of results for all models. The relative loading values were plotted against the average value of log(N_f). Error bars show one standard deviation.

Table 2: Average values for relative Young's modulus, fraction of failed elements, and number of cycles to failure for each fatigue stress.

$\Delta\sigma/E$ (%)	Average relative Young's modulus E/E_0 at failure (-)	Average percent fractured struts at failure (%)	Average number of cycles to failure N_f (cycles)
1	0.83	1.80	2.36×10^{13}
3	0.83	1.82	1.18×10^{8}
5	0.82	1.87	7.98×10^{6}
7	0.83	1.93	1.28×10^{6}
10*	0.82	1.77	5.40×10^{4}

*The results for the fifth model were not included at the 10% fatigue stress level.

We obtained constants C_{Vor} for each model and extended the results to relative densities for trabecular bone (ρ^*/ρ_s=0.3). The new values for cycles to failure, scaled for relative densities more appropriate to trabecular bone, were plotted against the normalized stress ranges. Power law curves were fit to the data for the new relative densities (table3).

Table 3: Calculated cycles-to-failure as a function of stress for different relative densities [$\log N_f = A + B\log(\Delta\sigma/E)$]

Relative Density, ρ/ρ_s	A	B
0.001*	-0.4900	-8.651
0.04**	-1.022	-8.651
0.15**	-1.213	-8.651
0.20**	-1.255	-8.651
0.30**	-1.313	-8.651

*Results from FEA analysis.
**Computed using constants from dimensional argument.

We compared our results for the 3D model at a relative density ρ/ρ_s=0.30 to experimental and computational results from other studies (figure 18). The 3D Voronoi model predicts higher cycles-to-failure for the 0.005-0.04 normalized stress range compared to the 2D hexagonal honeycomb model for fatigue crack growth. We also compared the projected results for the 3D model at relative density ρ/ρ_s=0.30 to the 2D hexagonal honeycomb analytical creep solution (Andrews et al, 1999; Guo et al, 1993) and to experimental results for compressive fatigue of bovine trabecular bone (Bowman et al, 1998).

To compare the results for creep in a 3D model, we used an expression for the creep strain rate in a foam (Andrews et al, 1999) with relative density, ρ^*/ρ_s=0.30:

$$\frac{\dot{\varepsilon}}{\dot{\varepsilon}_0} = \frac{0.6}{(n_s+2)}\left(\frac{1.7(2n_s+1)}{n_s}\frac{\sigma^*}{\sigma_0}\right)^{n_s}\left(\frac{\rho_s}{\rho^*}\right)^{\frac{3n_s+1}{2}} \tag{23}$$

where n_s is a creep material constant. We assumed the following creep behavior for the trabecular tissue:

$$\varepsilon = A_s\sigma^{n_s} \tag{24}$$

where A_s is a creep material constant. We used the material constants for bovine cortical bone as was done in Guo's two-dimensional creep model: $A_s=10^{-43.8}$ and $n_s=18.9$. Failure corresponded to a 5% strain and the number of cycles to failure were determined from the time to failure, t_f by assuming a frequency of 2 Hz. These assumptions are consistent with Guo's fatigue model. The resulting equation,

$$N_f = 2.098\times10^{-38}\cdot\left(\frac{\Delta\sigma}{E}\right)^{-18.9} \tag{25}$$

was plotted for comparison with the experimental data and the results of the other models.

Our model predicts higher cycles-to-failure than the experimental data showed for the same stress ranges. However, the 3D Voronoi fatigue model provides a better approximation of the slope of the experimental data than the hexagonal model.

4.4 Discussion

Obvious architectural limitations exist in our model of trabecular bone. We modeled the structure as a network of beam elements, each trabecular strut represented by a series of cylindrical rods. Trabecular bone appears as a combination of rods and plates, a cellular solid which is part open and partially closed. Our model also failed to represent the anisotropy present in bone by ignoring remodeling which occurs due to aging and external loading (Mosekilde et al, 1985).

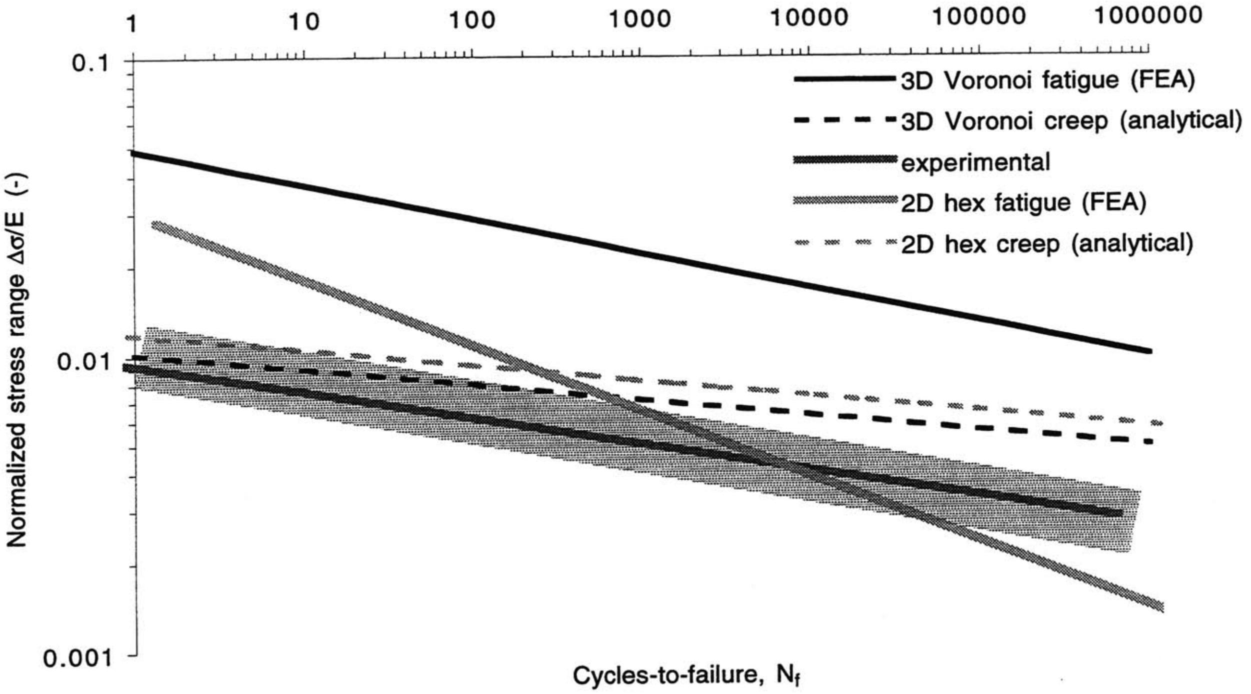

Figure 18: FEA results for fatigue of the 3D Voronoi model (ρ/ρ_s=0.30) were compared to results reported from previous studies. We plotted the linear regression fitting experimental data for compressive fatigue of bovine trabecular bone [$N_f=1.77 \times 10^{-23}(\Delta\sigma/E_0)^{-11.19}$] (Bowman et al, 1998) on a log-log scale. The shaded region approximates scatter in the data. Equations for curves from FEA of creep and fatigue (Andrews et al, 1999; Guo et al, 1993) of a hexagonal honeycomb model (ρ/ρ_s=0.30) for trabecular bone were also plotted. A plot of an analytical expression for creep in a three dimensional foam (ρ/ρ_s=0.30) was included for comparison (Andrews et al, 1999).

Our model suggests that microcrack growth contributes to failure in compressive fatigue. The three dimensional Voronoi model gives a better prediction of the slope of the S-N curve (-8.651 compared to –11.19 from experimental results) than the two-dimensional hexagonal honeycomb model. Previous studies suggest that other mechanisms such as creep may contribute to failure of trabecular bone at high stress ranges (Michel et al, 1993; Guo et al, 1993; Bowman et al, 1994; Bowman et al, 1998). Creep contributes to the fatigue behavior under cyclic loading at high stress in cortical bone (Carter and Caler, 1983; Caler and Carter, 1989). Although other studies have suggested a similar transition from fatigue-dominant to creep-dominant failure modes at around 100-1000 cycles for trabecular bone, our study indicates that fatigue plays a role for all stress levels.

Certain differences should be noted when comparing the model to previous studies. The hexagonal honeycomb modeled by Guo et al (1993) describes a two dimensional, anisotropic structure with members of wet bovine cortical bone (E_s=22.6 GPa) while our model represents a three dimensional random structure composed of elements of dry human trabecular bone (E_s=17.2 GPa). Guo's study set a 10% reduction in modulus (typically 15 fractured elements) as the specimen's failure criterion while our study did not report cycles-to-failure until the modulus had been reduced by 15% (typically 7 fractured members). Another critical difference between the two models lies in the assumed crack distributions. Guo assumed a beta distribution of crack lengths in his model while our study distributed an arbitrary number of uniform cracks throughout the model. We selected an initial crack length a/d=0.25 based on the average crack length observed in trabecular bone (Arthur, 1999). A better estimation of microcrack distribution in trabecular bone might improve our prediction for the cycles-to-failure.

When comparing our results to the experimental results of Bowman et al, consider that their study (1998) was conducted on wet bovine trabecular specimens over a range of relative densities and our study used a Young's modulus for the solid material that was consistent with dehydrated human trabecular bone (Rho et al, 1998). (Gibson lists Young's modulus values for individual trabeculae from various studies ranging from $0.76<E_s<14.1$ GPa (Gibson and Ashby, 1997).) Changing Young's modulus for the solid might lower the y-intercept for the three-dimensional Voronoi structure S-N curve. Note also that our results for the relative densities representative of trabecular bone were computed from FEA results for a relative density $\rho*/\rho_s=0.001$. A more accurate expression for Young's modulus of the solid and the scaling constants used to extend the FEA results to trabecular bone could significantly improve the correlation between our model and actual experimental results.

Our model presents several improvements over previous studies by introducing a three dimensional random structure. The dimensionality enabled us to account for bending, twisting, and tension in each of the trabecular elements. Despite these advances in our ability to model the fatigue behavior of bone, several limitations exist. We ignored trabecular thinning as a mechanism for weakening the structure. In addition, our analysis assumes that each strut either supports all of the applied external load or none of it. We did not account for the reduction of modulus in each individual trabecular strut as the crack length increased. We also assumed that crack growth proceeded from an initial crack length of 0.25d to a critical crack length of 0.75d along a linear propagation path. After a trabecular strut fractured and was removed, we continued the analysis to identify the next strut to fracture by assuming that all cracks in the model returned to the initial length. In other words, we assumed that crack propagation only occurred in the trabecular element for which fracture was imminent; once the element was removed from the mesh, crack growth in the next element to fracture would begin from the initial crack length and proceed until it reached the critical crack length. Without this assumption, we would need to compute new expressions for bending, tension, and twisting stress intensity factors for each element every time a member failed. For our initial conditions, Couroneau and Royer showed that only the type of loading and the Paris law exponent, assumed to be 4.5 for all trabeculae, influenced the crack propagation path for the model (1998). For a Paris constant m=4.5, initial crack lengths exceeding a/r=0.35 do not influence the results. Our crack lengths (a/r=0.5) satisfy this criterion.

4.5 Conclusions

This study demonstrates the use of the finite element method to predict fatigue behavior of trabecular bone using a three-dimensional random network of struts. Comparison with experimental data suggests that fatigue combines with creep to result in failure of trabecular bone under cyclic loading conditions at all stress levels.

Future work should focus on considering the effects of trabecular thinning and weakening of individual struts. Previous studies attempting to determine creep contributions to compressive fatigue behavior of bone could also be extended to three dimensions. Finally, the approach described in this study could be applied to study other open cellular solids like metallic foams.

4.6 References

Anderson TL. Fracture Mechanics. CRC Press, 1995; 69-72.
Andrews EW, Gibson LJ, and Ashby MF. The creep of cellular solids. *Acta Mat* 1999; in press.
Arthur TL. Private Communication March, 1999.
Arthur TL. Thesis proposal: Fatigue damage in trabecular bone. MIT, 1998.
Beaupre GS and Hayes WC. Finite element analysis of a three-dimensional open-celled model for trabecular bone. *J. Biomech. Eng.* 1985; **107**: 249-256.

Bowman SM, Guo XE, Cheng DW, Keaveny TM, Gibson LJ, Hayes WC and McMahon TA. Creep contributes to the fatigue behavior of bovine trabecular bone. *J. of Biomech. Eng.* 1998; **120**: 647-654.

Bowman SM, Keaveny TM, Gibson LJ, Hayes WC, and McMahon TA. Compressive creep behavior of bovine trabecular bone. *J. Biomech.* 1994; **27**: 301-310.

Burr DB, Forwood MR, Fyhrie DP, Martin RB, Schaffler MB, and Turner CH. Bone microdamage and skeletal fragility in osteoporotic and stress fractures. *J. Bone and Min. Res.* 1997; **12**: 6-15.

Burr DB, Turner CH, Naick P, Forwood MR, and Pidaparti RMV. Does microdamage accumulation affect the mechanical properties of bone? *Trans. ORS* 1995; **20**: 127-22.

Caler WE and Carter DR. Bone creep-fatigue damage accumulation. *J Biomech.* 1989; **22**: 625-635.

Carter DR and Caler WE. Cycle-dependent and time-dependent bone fracture with repeated loading. *J. Biomech. Eng.* 1983; **105**: 166-170.

Ciarelli TE, Schaffler MB, and Goldstein SA. Age effects on the fatigue behavior of human vertebral cancellous bone. *Trans. ORS.* 1999; **24**: 772.

Couroneau N and Royer J. Simplified model for the fatigue growth analysis of surface cracks in round bars under mode I. *Intl. J. Fatigue* 1998; **20**: 711-718.

Crandall SH, Dahl NC, and Lardner TJ. An Introduction to the Mechanics of Solids. Mcgram-Hill, Inc, 1978; 446.

Ding M, Odgaard A, Lind F, and Hvid I. Age variations in the microstructure of human tibial cancellous bone. *Trans. ORS.* 1999; **24**: 553.

Gibson LJ and Ashby MF. Cellular Solids Structure and Properties. Cambridge University Press, 1997; 436.

Gibson LJ. Private Communication April, 1999.

Gibson LJ. The mechanical behavior of cancellous bone. *J. Biomech.* 1985; **18**: 317-328.

Guo XE, McMahon TA, Keaveny TM, Hayes WC, and Gibson LJ. Finite element modeling of damage accumulation in trabecular bone under cyclic loading. *J. Biomech.* 1994; **27**: 145-155.

Huja SS, Katona TR, Burr DB, Garetto LP, and Roberts WE. Microdamage in fatigue loaded bone types surrounding endosseous implants. *Trans. ORS* 1999; **24**: 748.

Jensen JK, Mosekilde L, and Mosekilde L. A model of vertebral trabecular bone architecture and its mechanical properties. *Bone* 1990; **11**: 417-423.

Kraynik AM, Neilsen MK, Reinelt DA, and Warren WE. Foam Micromechanics: Structure and Rheology of Foams, Emulsions, and Cellular Solids. Proceedings of the NATO Advanced Study Institute on "Foams, Emulsions, and Cellular Materials." Kluwer, 1997.

Lee TC. Detection and accumulation of microdamage in bone. Trinity College, Dublin, Ireland 1997.

Levan A and Royer J. Part-circular surface cracks in round bars under tension, bending and twisting. *Intl J Fract* 1993; **61**: 71-99.

Michel MC, Guo XE, Gibson LJ, McMahon TA, and Hayes WC. Compressive fatigue behavior of bovine trabecular bone. *J. Biomech.* 1993; **26**: 453-463.

Mosekilde L, Viidik A, and Mosekilde L. Correlations between the compressive strength of iliac and vertebral trabecular bone in normal individuals. *Bone* 1985; **6**: 291-295.

Mosekilde L. Age-related changes in vertebral trabecular bone Architecture—Assessed by a New Method. *Bone* 1988; **9**: 247-250.

Mosekilde L. Sex differences in age-related loss of vertebral trabecular bone mass and structure-biomechanical consequences. *Bone* 1989; **10**: 425-432.

Murakami Y. Stress Intensity Factors Handbook. Pergamon Books Ltd, 1987.

Paris PC and Erdogan F. *Trans. ASME* 1963; **85**: 528.

Reilly GC and Currey JD. The development of microcracking during fatigue cycling in an equine radius loaded in vitro. *Trans. ORS* 1999; **24**: 479.

Rho JY, Roy ME, Tsui TY, and Pharr GM. Elastic properties of microstructural components of human bone tissue as measured by nanoindentation. *J. Biomed. Mat. Res.* 1999; **45**: 48-54.

Rooke DP and Cartwright DJ. Compendium of Stress Intensity Factors. Cvoron, 1976.

Schaffler MB, Boyce TM, and Fyhrie DP. Tissue and matrix failure modes in human compact modes during tensile fatigue. *Trans. ORS* 1996; **21**: 57-10.

Schiller AL. Bones and Joints. Pathology, ed. E Rubin and JL Farber. Lippincott, 1994.

Schulmeister V, van der Burg MWD, van der Giessen E, and Marissen R. A numerical study of large deformations of low-density elastomeric open-cell foams. *Mech. of Mat.* 1998; **30**: 125-40.

Silva MJ and Gibson LJ. Modeling the mechanical behavior of vertebral trabecular bone: effects of age-related changes in micro-structure. *Bone* 1997; **21**: 191-9.

Snyder BD, Piazza S, Edwards WT, and Hayes WC. Role of trabecular morphology in the etiology of age-related vertebral fractures. *Calcif. Tissue. Int.* 1993; **53 Supp. 1**: S14-S22.

Taylor D and Lee TC. Measuring the shape and size of microcracks in bone. *J. Biomech.* 1998; **31**: 1177-1180.

van der Burg MWD, Shulmeister V, van der Geissen E, Marissen R. On the linear elastic properties of regular and random open-cell foam models. *J. Cell. Plas.* 1997; **33**: 31-54.

Vashishth D, Behiri JC, and Bonfielld W. Crack growth resistance in cortical bone: concept of microcrack toughening. *Trans. ORS* 1997; **30**:763-769.

Vashishth D, Behiri JC, Tanner KE, and Bonfield W. Toughening mechanisms in cortical bone. *Trans. ORS* 1996; **21**: 56-10.

Vashishth D, Koontz J, Qui S, Cannon-Lundin D, Schaffler MB, and Fyhrie DP. Characterization of diffuse damage in human trabecular bone. *Trans. ORS* 1999; **24**: 765.

Wright TM and Hayes WC. The fracture mechanics of fatigue crack propagation in compact bone. *J. Mat. Res. Symp.* 1976; **7**: 637-648.

5 Biographical Note

Surekha Vajjhala attended the Massachusetts Institute of Technology from 1992-1996. As a sophomore she was named an Ely Burchard Scholar by the School of Humanities and Social Sciences. In recognition of academic and leadership achievement, she received the Institute's nomination for the Beinecke Brothers Memorial Scholarship which she was awarded in 1995. In 1996 she became a member of the Sigma Xi Scientific Research Honor Society and Alpha Sigma Mu Materials Science and Engineering Honor Society.

After receiving the Bachelor of Science degree in Materials Science and Engineering, she spent one year as a consultant with the Information Technology practice at Ernst & Young, LLP Management Consulting in Vienna, Virginia. She returned to MIT in 1997 to pursue graduate studies in the Department of Materials Science and Engineering. She conducted her thesis work under the supervision of Professor Lorna Gibson at the Orthopedic Biomechanics Laboratory at Beth Israel Deaconess Medical Center and served for one year as the student representative to the Departmental Committee on Graduate Students.

In January, 1999 she joined Molecular Geodesics, Inc. (MGI), a biomimetic materials start-up in Boston, Massachusetts. After completing the Master of Science degree in June 1999, she will continue her work in research and development of microstructural architectures for industrial and biomedical applications with MGI.

APPENDIX: Deriving a stress analysis factor for a semi-circular surface crack on a trabecular strut

For each trabecular strut, we can compute the strain energy release rate, G (Anderson, 1995) using the equation

$$G = \frac{K_I^2}{E} + \frac{K_{II}^2}{E} + \frac{K_{III}^2}{2\mu}, \qquad \text{(A.1)}$$

where K_I, K_{II}, and K_{III} are the opening, tearing, and twisting mode stress intensity factors for a surface crack on a cylindrical beam.

The shear modulus μ is given by:

$$\mu = \frac{E}{2(1+\nu)},$$

where ν is Poisson's ratio for the solid.

The strain energy release rate can be used to determine an effective stress intensity factor for the opening mode:

$$G = \frac{K_I^2}{E}, \text{ or}$$

$$K_{I,eff} = \sqrt{GE}.$$

Substituting equation A.1 for G, we get:

$$K_{I,eff} = \sqrt{K_I^2 + K_{II}^2 + K_{III}^2(1+\nu)}. \qquad \text{(A.2)}$$

Previous studies give the stress intensity factors for semi-circular surface cracks on cylindrical beams (Levan and Royer, 1993; Murakami, 1987):

$$K_I^B = 0.513\sigma_b\sqrt{\pi a} \qquad \text{(A.3)}$$

$$K_I^T = 0.758\sigma_t\sqrt{\pi a}$$

$$K_{III} = -0.325\tau_m\sqrt{\pi a},$$

where K_I^B and K_I^T are stress intensity factors for the opening mode under bending and tension, respectively. For the selected crack geometry, the stress intensity factor for the tearing mode $K_{II}=0$ at the crack front.

The bending moment σ_b, axial stress σ_t, and twisting moment τ_m can be calculated using data obtained from FEA:

$$\sigma_b = \frac{4\sqrt{SM_1^2 + SM_2^2}}{\pi r^3} \tag{A.4}$$

$$\sigma_t = \frac{SF_1}{\pi r^2}$$

$$\tau_m = \frac{2SM_3}{\pi r^3},$$

where SM_1 and SM_2 are the bending moments about two orthogonal normal axes, SM_3 is the twisting moment about the transverse axis, and SF_1 is the beam axial force.

We combine K_I^B and K_I^T to obtain K_I:

$$K_I = K_I^B + K_I^T. \tag{A.5}$$

Replacing K_I by the relationship above and noting that $K_{II}=0$, equation A.2 becomes:

$$K_{I,eff} = \sqrt{(K_I^B + K_I^T)^2 + K_{III}^2(1+\nu)}. \tag{A.6}$$

Substituting the relations from A.3, we get

$$K_{I,eff} = \sqrt{(0.513\sigma_b + 0.758\sigma_t)^2 + (-0.325\tau_m)^2(1+\nu)} \cdot \sqrt{\pi a}. \tag{A.7}$$

Finally, after using the relations from A.4 and simplifying, we get:

$$\Delta K_{I,eff} = \sqrt{((A+B)^2 + C)}\sqrt{a},$$

where

$$A = \frac{(0.513 \times 4)}{r^3}\sqrt{\frac{SM_1^2 + SM_1^2}{\pi}},$$

$$B = \frac{(0.758)SF_1}{r^2\sqrt{\pi}}, \text{ and}$$

$$C = \left(\frac{(-0.325 \times 2)SM_3}{r^3}\right)^2\left(\frac{1+\nu}{\pi}\right).$$

3734-10